DOE/ET/15611-T2
(DE81025560)

A HIGH MAGNETIC FIELD MHD GENERATOR PROGRAM

Quarterly Report for the Period January 1—March 31, 1981

By
C. H. Kruger
R. H. Eustis
M. Mitchner
S. A. Self
J. K. Koester
T. Nakamura

April 1981
Date Published

Work Performed Under Contract No. AC01-80ET15611

Stanford University
Stanford, California

U. S. DEPARTMENT OF ENERGY

DISCLAIMER

DISCLAIMER

Available from the National Technical Information Service, U. S. Department of Commerce, Springfield, Virginia 22161.

Price: Printed Copy A05
Microfiche A01

DOE/ET/15611-T2
(DE81025560)
Distribution Categories UC-90g and UC-93

A HIGH MAGNETIC FIELD MHD GENERATOR PROGRAM

QUARTERLY REPORT

for the period

January 1, 1981 - March 31, 1981

Stanford University
Stanford, California 94305

Date Published - April 1981

Prepared for

THE UNITED STATES DEPARTMENT OF ENERGY

Under Contract DE-AC01-80ET15611

THIS PAGE

WAS INTENTIONALLY

LEFT BLANK

ABSTRACT

This report describes progress in an experimental and theoretical program designed to investigate MHD channel phenomena which are important at high magnetic fields. The areas of research include nonuniformity effects, boundary layers, Hall field breakdown, the effects of electrode configuration and current concentrations, and studies of steady-state combustion disk and linear channels in an existing 6 Tesla magnet of small dimensions.

In the study of the effects of nonuniformities, experiments have been performed to test a multi-channel, fiber optics diagnostic system that yields time-resolved temperature profiles in an MHD channel. For the study of magneto-acoustic fluctuation phenomena, a one-dimensional model has been developed to describe the performance of a non-ideal MHD generator with a generalized electrical configuration.

The installation of the hardware for the data acquisition and reduction of the laser Doppler velocimeter data, to be used in the study of turbulence suppression in a magnetic field, has been nearly completed and preliminary software has been written.

A two-dimensional MHD computer code has been developed which predicts the dependence on electrode and insulator dimensions of the onset of interelectrode Hall field breakdown, as initiated either by breakdown in the insulator or in the plasma. There is good agreement between calculation and measurements.

Calculations have been performed of the effects of nonuniformities on the flow and electrical behavior of baseload-sized disk generators. Also, predictions of the performance of baseload inflow disk generators have been calculated and compared with linear generators.

TABLE OF CONTENTS

LIST OF FIGURES

LIST OF TABLES

1.0 INTRODUCTION

This report describes progress and results for the most recent quarter of the research program, "A High Magnetic Field MHD Generator Program," conducted by the High Temperature Gasdynamics Laboratory at Stanford University under Contract DE-AC01-80-ET15611 with the Department of Energy. The program is directed to a number of important problems in MHD generator channels, and in particular to effects associated with high mgnetic fields and interaction parameters. The research is primarily experimental in nature, with the use of advanced diagnostics methods and coordinated theoretical and numerical studies for the interpretation of the data and application of the results to large-scale generators. It is intended to provide supporting research for MHD hardware development in areas where performance limitations and design constraints are not now adequtely understood.

The research program is divided into three major areas:

Work Area I - Plasma nonuniformities and instabilities

Work Area II - Boundary layer and Hall field phenomena

Work Area III - Six Tesla magnet investigations.

Work Area I involves the effects on generator performance of nonuniformities, including those caused by acoustic and other waves in the MHD channel. Progress in an experimental program to measure the performance effects of controlled nonuniformities introduced in the MHD generator plasma is described in Section 2.0. Present results of an analytic and experimental study of magneto-acoustic waves and their growth and attenuation rates as a function of generator conditions and magnetic field are also reported in this section.

In Work Area II, the development and testing of an improved laser doppler anemometer for the measurement of turbulence damping and resultant effects on MHD boundary layers are discussed in Section 3.0. Results of studies of insulator and plasma induced Hall field breakdown are presented in Section 4.0.

An existing 6 Tesla superconducting magnet has been used in Work Area III for small-scale experiments at high magnetic fields. Studies of the fluid and electrical behavior, and of the performance of baseload inflow disk generators are reported in Section 5.0.

2.0 NONUNIFORMITIES AND INSTABILITIES

2.1 Nonuniformity Investigation

Losses incurred in experimental MHD devices due to core and wall nonuniformities exceed the levels predicted by simple one-dimensional theories of generator performance. By nonuniformities is meant variations within the plasma of temperature or seed species concentrations which result in variations of important plasma transport properties. These properties, such as electrical conductivity and Hall parameter, are critical factors in an effective Ohm's law for a MHD device. The nonuniformities may be a consequence of plasma contact with cooled surfaces, such as channel walls, of incomplete combustion in upstream components, or of uneven seed distribution.

Theories which model the plasma in two and three dimensions and predict the effects of various geometries of nonuniformity structures within the plasma abound, the best known perhaps being Rosa's analysis [2.1] of a layered medium. This profusion of nonuniformity models for MHD plasmas points out the need for background data to provide a yardstick with which these models may be compared and evaluated. The insights brought about by the comparison of theory to data will aid designers of power-plant scale MHD generators in maximizing the efficiency of their designs.

At Stanford, a study is in progress to provide some of this background data and to compare these observations to some existing theories. The experimental program proposes to observe changes in electrical performance of a linear MHD device with and without the presence of a nonuniformity of known extent and degree in the active region of the device. The investigation may be considered in three stages:

- Characterization of a background plasma.
- Introduction of the nonuniformity and determination of its effect on local plasma transport properties.
- Measurement of the effects of the presence of the nonuniformity in terms of the electrical behavior of the MHD device.

The first stage of the investigation has been completed with results detailed in previous reports [2.2,2.3]. The second stage of the investigation may be further broken down into two more steps, the first including the design and testing of a device which will produce a nonuniformity of the desired structure and strength. This portion of the second stage has been completed and has also been described previously [2.3].

The next portion of the second stage involves the design and testing of a diagnostic which will measure in situ the effect on transport properties of the nonuniformity produced by the apparatus fabricated in the first portion. In this report is described the completion of this stage of the program and the plans for the third and final stage.

2.1.1 Design

The design of the diagnostic to perform the measurements of plasma transport properties has already been alluded to previously [2.4], and a brief recap is presented here.

It was decided to use potassium line reversal to measure plasma temperature in a plane perpendicular to the flow of the plasma as a means of characterizing the extent as well as the strength of the nonuniformity. A schematic of the design is shown in Fig. 2.1.

A tungsten filament lamp is imaged into the plasma by means of a projection lens and the illumination is modulated by a mechanical chopper. The lamp and plasma radiation are then focussed onto an array of six detectors mounted in line and oriented transverse to the flow of the plasma. An interference filter provides spectral resolution in the region of the K 7665 A line. An aperture stop determines the solid angle of radiation incident on the detectors from both the lamp and the plasma.

The detectors are silicon photodiodes with active areas 2.54 mm (0.1 in) in diameter, which act as the field stops for each detector. The spacing of the detectors determines the region of plasma each

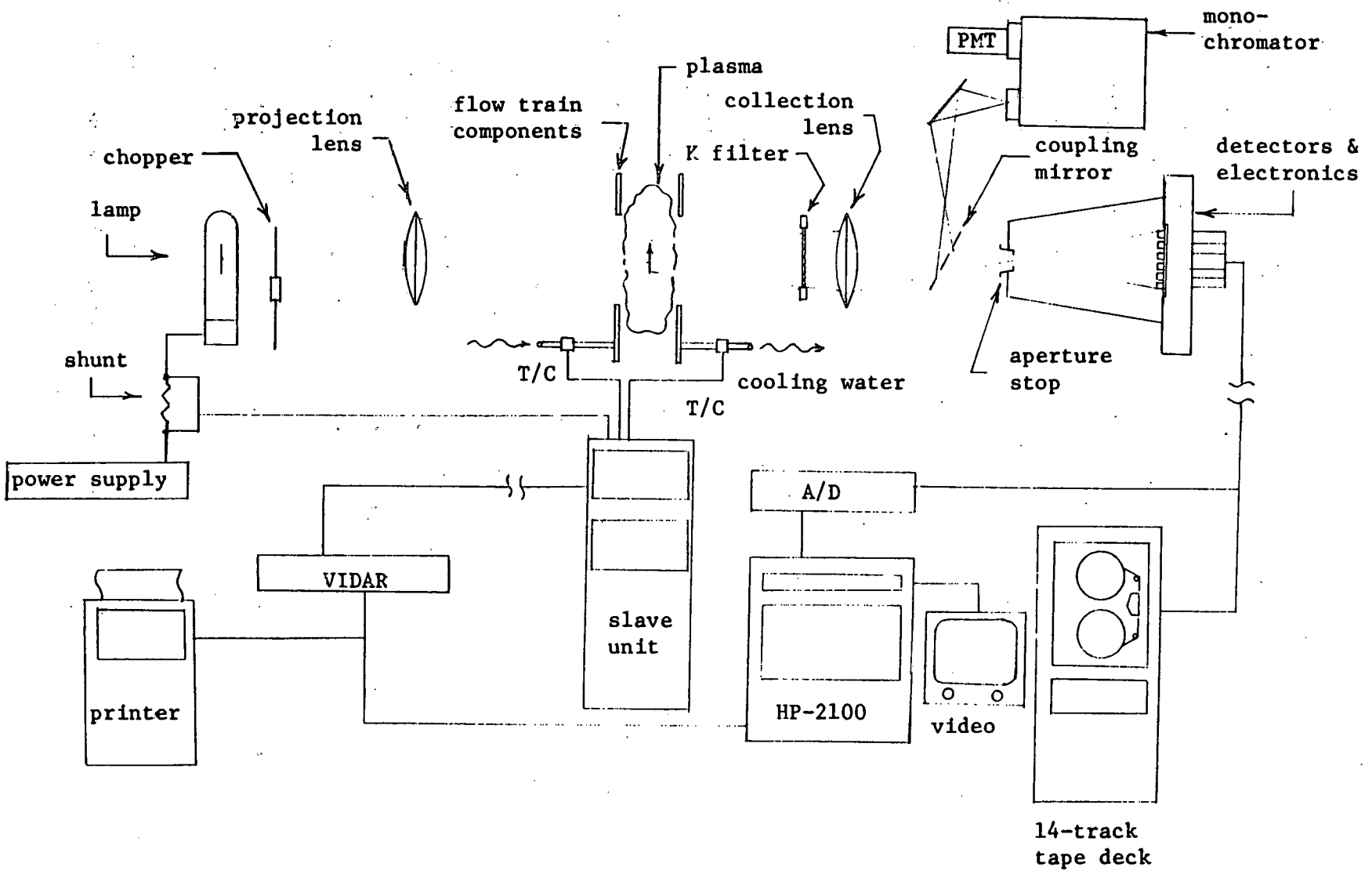

Figure 2.1 Diagnostic and data acquisition schematic.

detector observes, the only requirement being that each region must also be transilluminated by the lamp. Each detector has associated with it individual amplifying and buffering electronics to insure efficient transmission of the signals over long lead distances.

The diagnostic works on the same technique as the Soviet automated line reversal device [2.5] which makes use of the algorithm

$$T_p = T_L \left\{1 + \frac{\lambda_c T_L}{c} \ln \left[\frac{V_p + V_L - V_{L+p}}{K_1 (V_p - n)}\right]\right\}^{-1} .$$

where T_p = plasma reversal temperature, K
T_L = lamp brightness temperature, K
λ_c = center wavelength for the device, m
c = constant = .014384 m`K
V_p = detector signal from plasma alone, volts
V_L = detector signal from lamp alone, volts
V_{L+p} = detector signal from lamp plus plasma, volts
K_1 = constant associated with projection optics
n = DC offset for each detector, volts

In the Soviet device, the lamp temperature T_L is evaluated from a secondary lamp continuously through the collection optics by means of a beam splitter, secondary optical train, and a second chopper which modulates the lamp radiation in phase with the primary lamp chopper. This necessitates careful alignment of the secondary lamp as well as the assumption that the variations in both lamps are identical. The diagnostic used for nonuniformity experiments at Stanford uses a precision shunt (see Fig. 2.1) to monitor lamp current and a pre-test calibration of lamp brightness temperature vs. current to provide continuous monitoring of the lamp temperature, T_L.

The center wavelength λ_c of the device is determined by the angle of the K filter with respect to the optical axis. A pre-test calibration of the transmission function of the K-filter together with the aperture stop is performed by coupling a monochromator into the optical system as shown in Fig. 2.1. This procedure provides a curve relating

filter angle to the peak transmission wavelength, λ_c of the optical system.

The detector signals occurring when the lamp radiation is blocked and unblocked by the chopper correspond to the voltages V_p and V_{L+p}, respectively. The detector signal resulting from the lamp radiation alone cannot be provided during the test, since it is impossible to remove the plasma and then re-install it in the channel with the frequency desired. Instead, pre- and post-test calibrations are performed with the lamp at various currents and the K-filter at various angles. The signals from each detector for these conditions are then used to construct a three-dimensional matrix which relates filter angle and lamp current during the test to a signal level from the detector. The post-test calibration provides a measure of how the matrix elements have changed over the course of the test. It is assumed in calculating V_L that the variation of calibration arrays is linear with time.

Each detector has associated with it a DC offset, n, due to amplifier drift. This offset is accounted for by measuring the detector signals with no incident radiation just prior to performing a temperature measurement. It is assumed that the DC offset does not vary significantly over the ~ 30 second period of a single measurement.

The diagnostic as described above has a frequency response limited by the modulation of the lamp radiation by the chopper and the frequency response of the detector/amplifier circuitry. To date that upper limit has been approximately 4000 Hz.

Real-time data acquisition is provided by a 14-track analog tape deck for recording detector signals and an A/D converter linked with a HP2100 minicomputer for on-line data reduction. Time-averaged thermocouple data are recorded by a VIDAR IDVM and slave unit for post-test heat balance calculations.

2.1.2 Testing

Testing of the line reversal diagnostic to date has included four runs; the first three associated with debugging the diagnostic design, hardware and the conventional run apparatus, respectively. The most significant amount of time and effort was involved in detecting and correcting defects in some of the optical components which caused the experimental results to appear anomalous for one of the tests. The fourth test was conducted with a monochromator adjacent to the diagnostic (see Fig. 2.1) which could be coupled to the optical train and used to perform spectral scans of the 7665-7700 A potassium doublet and line reversal measurements at various run conditions. This parallel detection system provided a check on the plasma behavior as well as on the quantitative performance of the diagnostic.

A schematic of the flow train used for the fourth test is shown in Fig. 2.2. This flow train consisted of the M-2 combustor and plenum and a run-in section whose inside wall dimensions at the exit were the same as those of the M2 channel, which will be the test section used in upcoming electrical tests. The run-in section exhausts approximately 12 in (300 mm) upstream of a duct which transferred the combustion products to a scrubber and finally to the atmosphere. A blower on the downstream ducting provided sufficient suction to insure that no combustion products escaped to the room environment.

The diagnostic optical axis was oriented perpendicular to the plasma flow at the open portion of the train approximately 2 in (50 mm) downstream from the run-in section exit. The six detectors were positioned so that their images were centered vertically about the run-in section centerline. Center-to-center spacing of the image points in the plasma was about 0.4 in (10 mm) and each detector observed a region of the plasma about 0.1 in (2.5 mm) in diameter.

Plasma temperatures were measured at total mass flow rates of 0.15 lbm/sec (.068 kg/sec) and 0.25 lbm/sec (.113 kg/sec) and N_2/O_2 ratios ranging from 1.25 to 0.25. In these experiments, nitrogen was added in the combustor as a diluent; the N_2/O_2 ratio has a significant effect

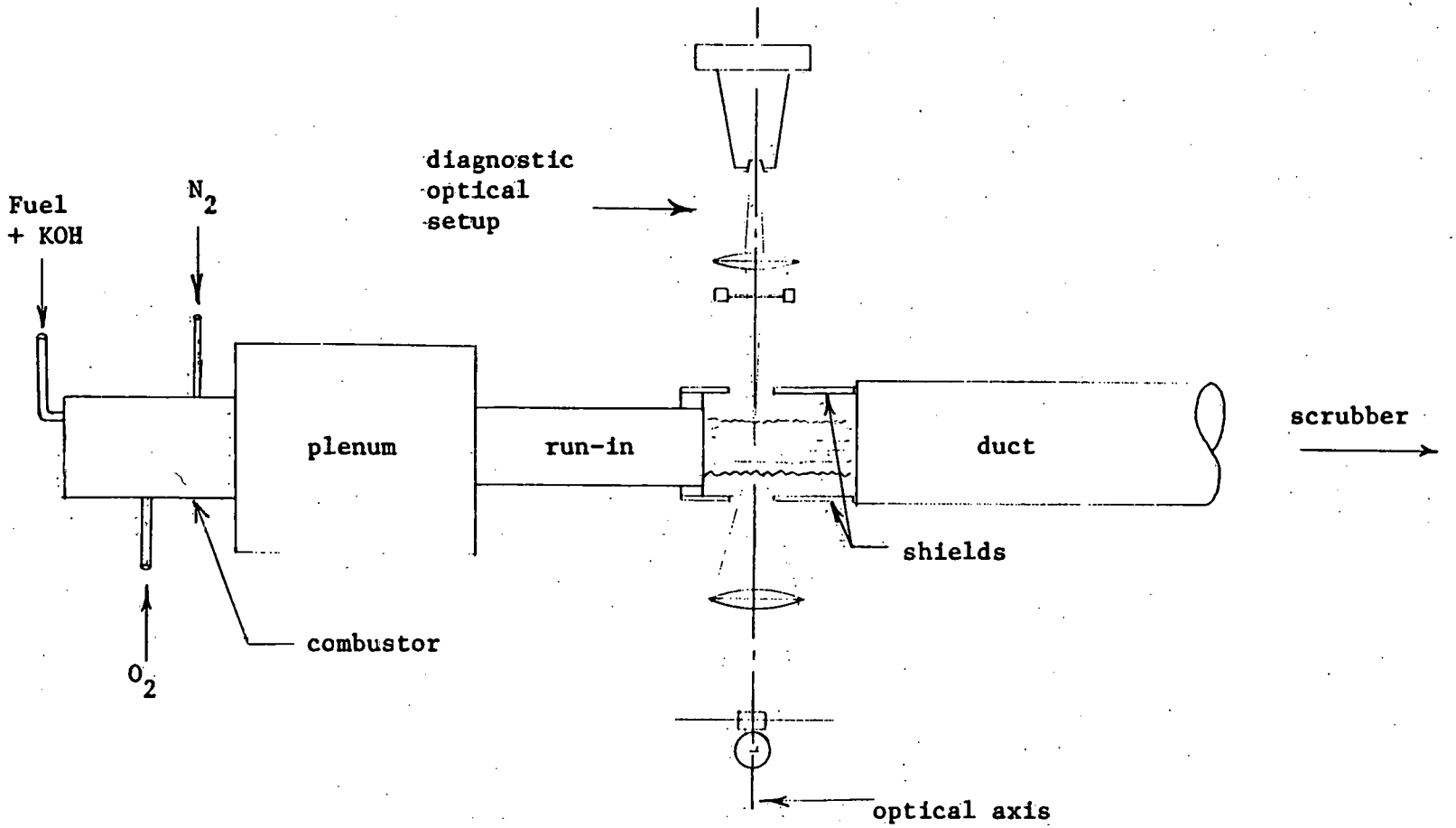

Figure 2.2 LRT2 flow train component schematic.

upon plasma temperature. At all run conditions, the mixture of fuel and oxygen was stoichiometric.

The results of a preliminary analysis of the data averaged over a period of approximately 1/2 second are shown in Fig. 2.3 for several run conditions. Also shown as dashed lines are temperatures calculated from equilibrium considerations and heat balance data.

The temperatures calculated from detector #5 have not been reported with these data because the values of #5 for each run condition are beyond the range of error due to experimental variations and are therefore suspect. It should again be pointed out that these results are preliminary.

It can be seen from Fig. 2.3 that, with the exception of detector #6, the temperature calculated from the detector signals are in good relative agreement, being in all cases (including #6) within ±2.5% of their averaged value; the variation is typically better than ±1% if detector #6 is excluded. The agreement to equilibrium predictions of temperature based on heat balance data is good for all cases with the exception of Run 110 ($\dot{m}$ = 0.15, N_2/O_2 = 1.25), being within about 2% for all detectors if, again, #6 is excluded. The equilibrium temperature for Run 110 is based on measurements taken at the beginning of the test. The cooling water temperature changes through the flow train components do not take into account the heat capacity of the MgO brick used for lining and protecting the components. At the start of the test, it is thought that the considerable heat capacity of these bricks as the plasma temperatue increases causes some uncertainty in the heat balance calculations. Also, at such relatively low plasma temperatures, the signal levels are significantly lower than conditions with hotter plasmas. This results in less confidence in the absolute accuracy of the measurements than for similar measurements made with the higher intensities caused by hotter plasmas.

The temperatures calculated from detector #6 are almost consistently higher than temperatures from the other four detectors at the higher total mass flow rates. No clear explanation has been identified

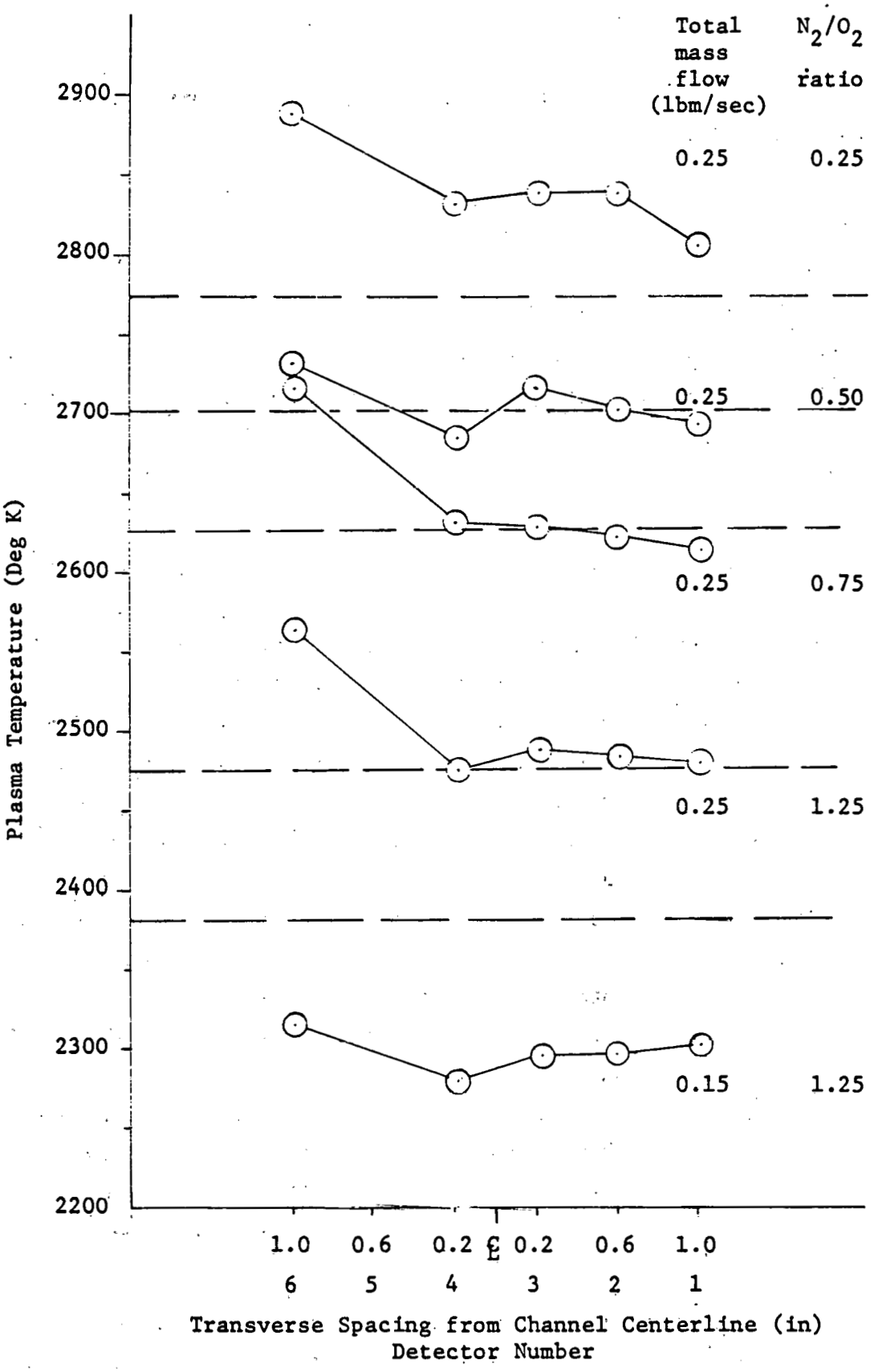

Figure 2.3 Preliminary results of diagnostic test LRT2.

as yet for this trend. Possibilities include nonlinear variations in the calibration matrices and optical alignment variations arising from distortion of the metal supporting members exposed to the intense radiation of the hot plasma.

From this analysis, it can be seen that, with some exceptions, measurements made with the present diagnostic design show good relative agreement and reasonably good agreement with temperatures predicted from equilibrium consideraions. Explanations for the observed anomalous behavior of detector #5 are being sought, as well as possible reasons for the relative variations of detector #6. Taken together, the results of this test point to a diagnostic which will be a suitable tool for the forthcoming experiments.

2.1.3 Further Work

As previous tests have not been performed in a magnetic field, the next development will be to modify the diagnostic structurally to fit into the tight quarters of the Stanford 2.7 T magnet, both in an upstream and downstream configuration. Other modifications will improve S/N by enlarging the aperture stop diameter and by raising the voltage output limit of the detectors.

The next experiment should include the coupling of the nonuniformity injector with the M2 channel and detection of the extent of the resultant wake structure by the diagnostic. This test is presently envisioned as two sets of runs, both in the 2.7 T magnet but without electric or magnetic fields. One set would have the line reversal diagnostic in a position to view the nonuniformity upstream of the active region over a range of flow conditions. The second set would have the diagnostic in the downstream position and the same range of flow rates. Combining the results of both sets of runs should provide a picture of how the nonuniformity diffuses outward over a range of plasma velocities and temperatures, assuming all components work to satisfaction.

The final experiment would again consist of a set of two identical runs with the diagnostic first in the upstream and then the downstream positions, this time in the presence of electric and magnetic fields. This set of tests would be performed over a wide range of flow rates and N_2/O_2 ratios in order to provide a useful body of background data for comparison to theories.

The final step in this experimental program is to provide some comparisons of existing theories to the data accumulated in the final tests. In addition, an engineering model of a nonuniform plasma will be proposed which is based loosely on Rosa's analysis of a layered plasma. Comparison of these models with the data will hopefully provide quantitative insight into the effects in MHD devices due to core nonuniformities. The concluding step will be a logical extension of the more promising models to the case of a large-scale MHD generator and the identification of probable trends to be expected.

2.2 Magneto-acoustic Disturbances

The one-dimensional, time-dependent MHD equations form the basis for the study of magneto-acoustic instabilities in a combustion MHD generator. The momentum and energy equations contain the MHD source terms $\vec{J} \times \vec{B}$ and $\vec{J}^2/\sigma$, respectively, which must be modelled. For the study of magneto-acoustic phenomena it is necessary to construct a model of the generalized electrical configuration and to include non-ideal effects such as boundary layers and electrode voltage drops. This is especially important in order to design an experiment for a smaller facility, such as the Stanford M2.

To incorporate the non-ideal effects, the model assumes a one-dimensional core flow in a channel with developing boundary layers, and general transverse and axial electrical connections. It is then assumed that the magneto-acoustic waves propagate axially only in the core region, and that they travel with a time scale that is fast with respect to the convective and conductive time scales in the boundary layers, so that the passing waves have a negligible influence on the boundary

layers. The non-ideal effects can then be incorporated by replacing the source terms with values representative of the core, to include implicitly the 2D and 3D effects.

Consider a periodic, segmented array of electrodes connected through a load R_s with applied batteries V_{Bs}, inclined at the diagonalization angle ϕ. An axial electrical connection allows current I_n to pass through load R_n and battery V_{Bn}, as shown in Fig. 2.4. The generalized Ohm's law equations,

$$J_x = \frac{\sigma}{1+\beta^2}(E'_y + \beta E_x) \tag{2.1}$$

$$J_y = \frac{\sigma}{1+\beta^2}(E_x - \beta E'_y) \tag{2.2}$$

and the axial and transverse circuit equations which result from applying Kirchoff's Law,

Transverse:
$$-V_{Bs} + I_s R_s = \int_{\substack{\text{transverse}\\ \text{load path}}} \vec{E} \cdot d\vec{\ell} \tag{2.3}$$

Axial:
$$-V_{Bn} + I_n R_n = \int_{\substack{\text{axial}\\ \text{load path}}} \vec{E} \cdot d\vec{\ell} \tag{2.4}$$

provide four equations from which the four unknowns (J_x, J_y, E_x, E_y), and hence the generator performance, can be determined if the local plasma properties are known.

In order to account for the 2D and 3D effects in a quasi-1D description, it is convenient to solve for the core electrical properties in the following manner:

1. Observe that in the core

$$J_{xc}/J_{yc} = m, \quad \text{a constant.} \tag{2.5}$$

This assumption evidences itself in 2D calculations, even with finite electrode segmentation, cf. Oliver [2.5]. Then, the other electrical properties can be expressed in terms of J_{yc} and m locally.

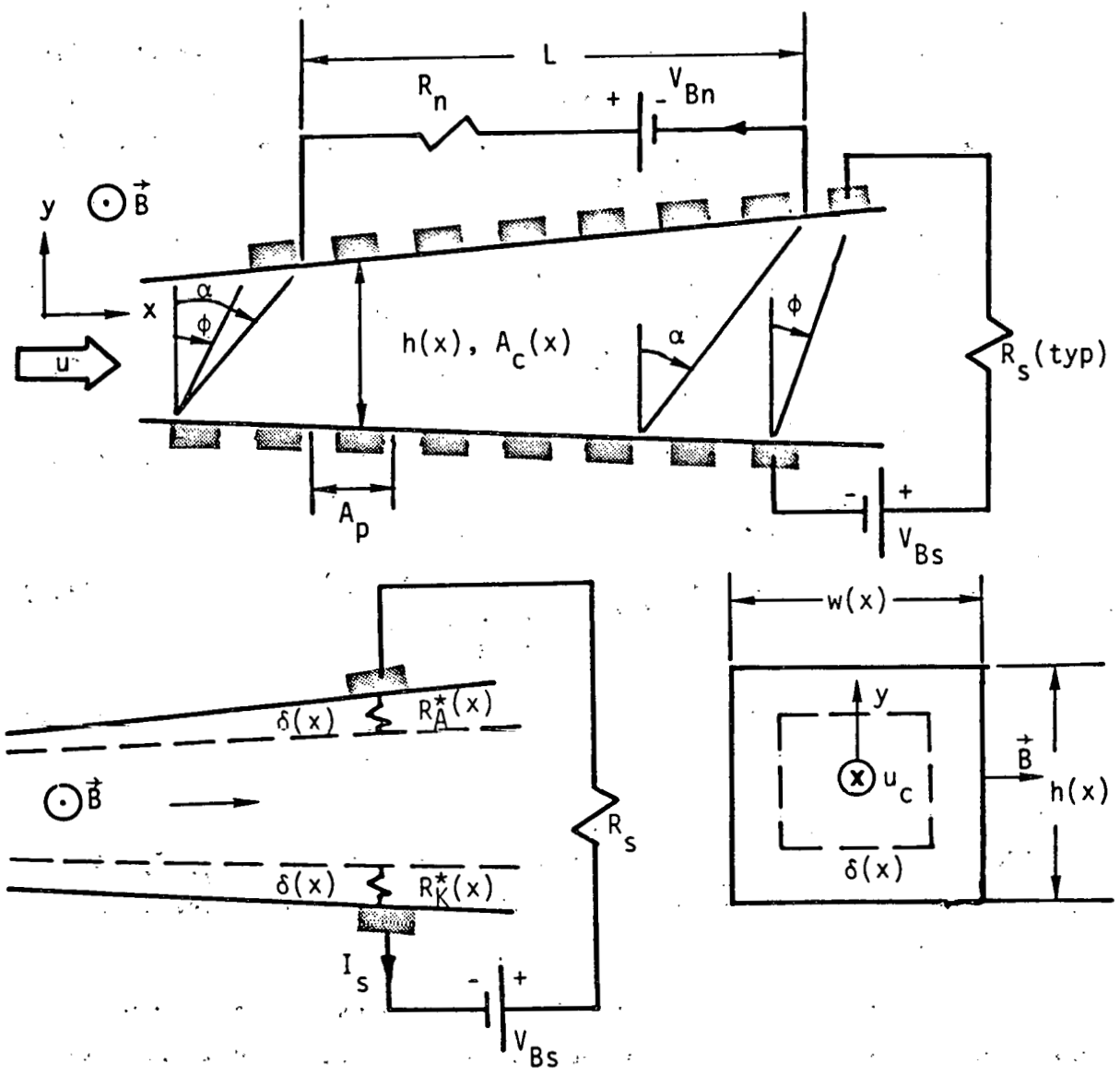

Figure 2.4 A representation of the MHD generator with generalized electrical connections and boundary layers used in the non-ideal quasi-one-dimensional model.

2. Utilize a form of the transverse circuit equation (2.3) to relate m and J_{yc}.

3. Observe that the axial circuit equation (2.4) cannot be evaluated directly if $A_c = A_c(x)$ and $E_x = E_x(x)$, etc. But current continuity can be used to derive an expression for I_n, which is invariant, in terms of J_{yc} and m.

4. The results of steps 3 and 4 can be used to find m and J_{yc} in terms of I_n, and thus the local properties in step 2 can also be expressed in terms of I_n.

5. Local property values and the results of step 5 can now be used in eq. (2.4) to solve for I_n, and thus all the other properties.

In step 2, currents can be summed over the control surface shown in Fig. 2.5. Assuming that properties do not vary substantially over the diagonal connection length and averaging in the spanwise (z) direction, the effect of the insulator wall boundary layers can be incorporated in an equation relating J_y and m.

$$J_y = \frac{\bar{\sigma}}{\sigma_c} J_{yc} + \frac{\sigma_c u_c B}{(1-\beta m)} \left(\frac{\bar{\sigma}}{\sigma_c} - \frac{\overline{\sigma u}}{\sigma_c u_c}\right) \tag{2.6}$$

The overbars indicate z-averages and the subscript c denotes core values.

Now consider the terminal voltage in the transverse circuits shown in Fig. 2.6 and sum the voltage drops using Eq. (2.3). Assuming that the variation of σ near the wall causes all quantities to be primarily dependent on y and J_y is constant in the boundary layer, it can be shown that

$$-J_{yc} = \frac{\langle u \rangle Bh + V_{Bs} + \frac{\sigma_c u_c B}{(1-\beta m)} \left(\frac{\bar{\sigma}}{\sigma_c} - \frac{\overline{\sigma u}}{\sigma_c u_c}\right) R_s^*}{\hat{R}_{KA}^* + R_c^* + R_s^* \frac{\bar{\sigma}}{\sigma_c}} \tag{2.7}$$

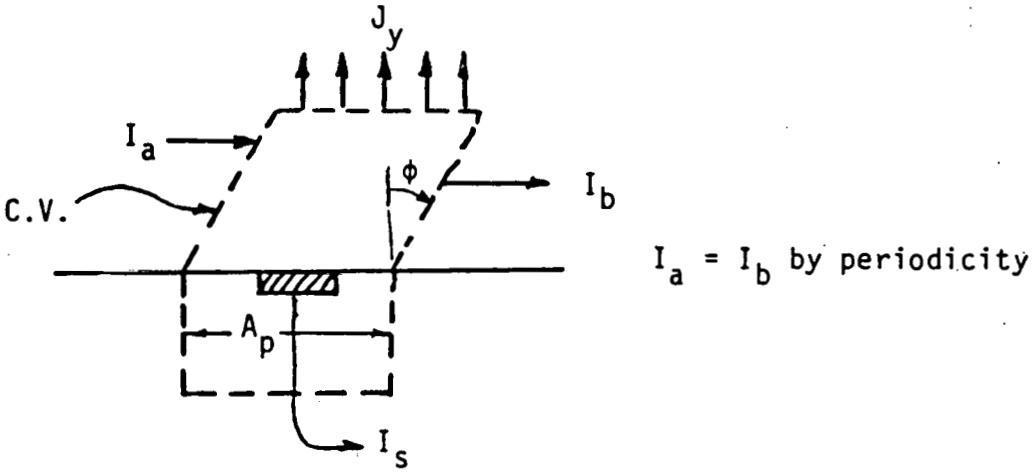

Figure 2.5 Transverse current control volume.

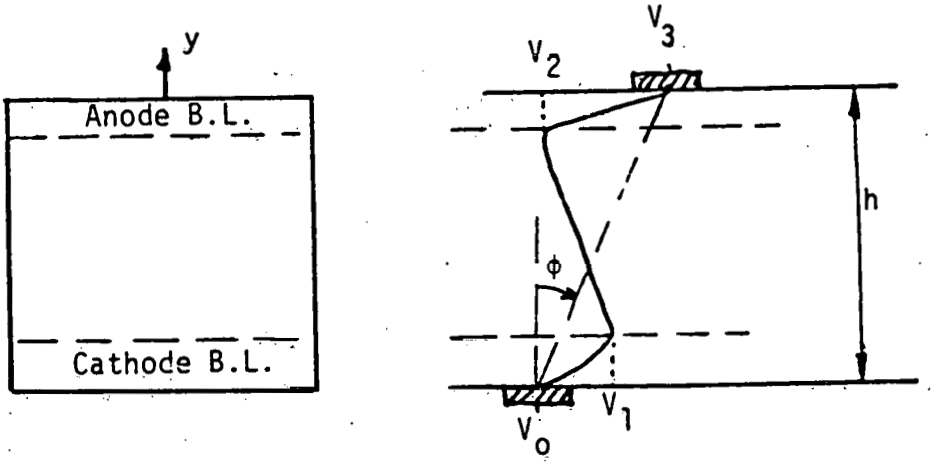

Figure 2.6 Transverse circuit voltages.

where

$$\hat{R}_K^* = \frac{\delta}{\sigma_c}(1+\beta^2)\left[\left\langle\frac{1}{\sigma}\right\rangle_{BL_K}\sigma_c - 1\right] , \tag{2.8}$$

$$\hat{R}_A^* = \frac{\delta}{\sigma_c}(1+\beta^2)\left[\left\langle\frac{1}{\sigma}\right\rangle_{BL_A}\sigma_c - 1\right] , \tag{2.9}$$

$$\hat{R}_{KA}^* = \hat{R}_K^* + \hat{R}_A^* , \tag{2.10}$$

$$R_s^* = \sigma_c R_s/h , \tag{2.11}$$

and

$$R_c^* = \frac{h}{\sigma_c}\left[(1-\beta m) + (m+\beta)\tan\phi\right] . \tag{2.12}$$

$\hat{R}_K^*$ and $\hat{R}_A^*$ are the effective resistances at the cathode and anode, respectively, and have no dependence on m or ϕ. Their sum, $\hat{R}_{KA}^*$, represents the extra boundary layer resistance, beyond that which would result if σ were uniform. $\hat{R}_c^*$ is the core resistance and $\hat{R}_s^*$ is the normalized load resistance. The quantities $\langle 1/\sigma\rangle_{BL}$ are effective conductivities in the boundary layers which can be calculated by a model for σ, or deduced from measured voltage drops.

In step 3, currents are summed over the control volume in Fig. 2.7, assuming that some electrodes exist past the curent take-off plane, which is at an equipotential inclined at angle α. The result relates the invariant axial current I_n to $\bar{J}_y$ and m according to the expression

$$\left\{2\frac{\delta}{h}\left[\frac{\langle\sigma\rangle_{BL}}{\sigma_c}(m+\beta) - \beta\right] + m\left(1 - \frac{2\delta}{h}\right) - \tan\phi\right\}\bar{J}_y = \frac{I_n}{wh} . \tag{2.13}$$

Equations (2.7) and (2.13) provide two equations relating $\bar{J}_y$, m, and I_n after Eq. (2.6) is used to eliminate J_{yc}. Thus, if the plasma properties are known, m and $\bar{J}_y$ (and hence J_{yc}) can be determined in terms of I_n.

Then, $E_{xc}(x)$, $E_{yc}(x)$, $J_{yc}(x)$, and $J_{xc}(x)$ can all be determined in terms of I_n and local plasma properties.

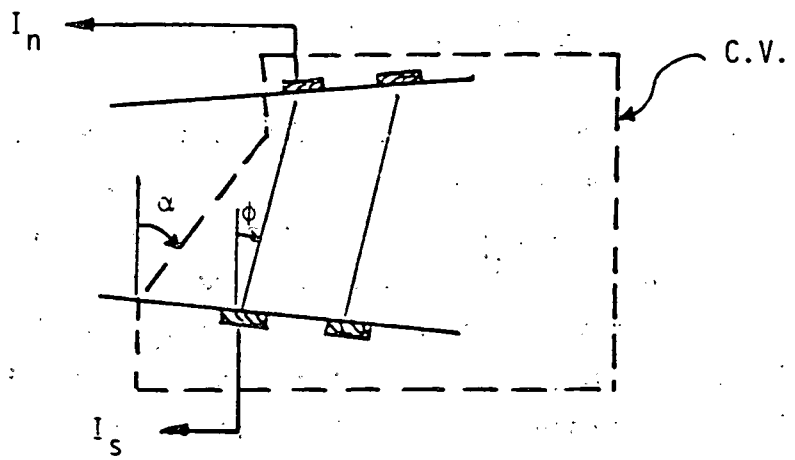

Figure 2.7 Axial current control volume.

Now the axial circuit equation can be utilized to determine I_n. Applying Kirchoff's Law again Eq. (2.4),

$$I_n\ (R_n + R_{KAn}) = V_{Bn} - \int_o^L E_{xc}(x,I_n)\ dx \tag{2.14}$$

R_{KAn} represents the total cathode plus anode boundary layer resistance, in analogy to the transverse circuit equation.

All quantities are known in Eq. (2.14), except for I_n. Thus, Eq. (2.14) allows I_n to be determined, possibly implicitly. For a Faraday generator $I_n = 0$. Thus Eqs. (2.6), (2.7) and (2.13) can be used to solve for $\overline{J}_y$ and m directly.

These steady state properties can now be perturbed to determine the source terms in the momentum and energy equations. Assuming that the angle of the current streamlines, m, is not appreciably affected by fluctuations,

$$(\vec{J} \times \vec{B})'_x = J'_{yc}\ B_o \tag{2.15}$$

$$(\vec{J}^2/\sigma)' = \frac{J_{yc}}{\sigma_c}\ (1+m^2)\ \left[2\ \frac{J'_{yc}}{J_{yc}}\ - \frac{\sigma'}{\sigma_c}\right] \tag{2.16}$$

Neglecting variations in the z-direction and allowing fluctuations in P, T, u, σ and β in the core, $\overline{J}_{yc}$ can be perturbed to yield

$$\frac{\overline{J}'_{yc}}{\overline{J}_{yc}} = \frac{(C_{ysc}\sigma_p + C_{yHc}\beta_p)P' + (C_{ysc}\sigma_T + C_{yHT}\beta_T)T' + u'/\overline{V}_s}{1 + \dfrac{\overline{J}_{yc}\sigma_c}{\Delta_{oc}h} \cdot \dfrac{\partial \hat{R}^*_{KAs}}{\partial \overline{J}_{yc}}} \tag{2.17}$$

where

$$C_{ysc} = \frac{M_o}{\overline{V}_{Bs}} - \frac{\overline{R}_{KAs} + \overline{R}_s}{\Delta_{oc}}$$

$$C_{yAc} = -\frac{(\tan\phi - m)\beta_c}{\Delta_{oc}}$$

$$\Delta_{oc} = \overline{R}_{KAs} + (1-\beta_c m) + (m+\beta_c) \tan \phi + \overline{R}_s$$

and

$$\overline{V}_s = - \left[M_o + \overline{V}_{Bs} \right]$$

In these equations,

$$\overline{J}_{yc} = J_{yc} / \sigma_c a_o B$$

and

$$\overline{R}_{KAs} = \frac{\sigma_c \hat{R}^*_{KA}}{h} , \quad \overline{R}_{KAn} = \frac{\sigma_c R^*_{KAn}}{L} , \quad \overline{R}_s = \frac{\sigma_c A_p R_s}{h} .$$

3.0 BOUNDARY LAYER PHENOMENA

3.1 Boundary Layer Diagnostics for Velocity Measurements

Laser Doppler Velocimetry (LDV) has been proven to provide reliable velocity measurements in the harsh environment of an MHD generator. An advanced LDV system is currently being developed at Stanford to measure the effect of turbulence suppression in a magnetic field. This system consists of two major subsystems: the optical components to provide the LDV measurements, and the data acquisition/reduction components to store and interpret the LDV data. Included in the latter subsystem is the necessary software to control the system. The optical components have been described in previous reports, while the data acquisition/reduction components will be described below.

During September and November of 1980, several tests were conducted in an MHD plasma to compare two different data acquisition/reduction systems: a frequency tracker system with an analog recording of data and a burst counter system with a digital recording of data. After comparing the two systems, it was determined that a counter-based system was superior to that with a tracker.

The burst counter selected (TSI model 1990A) operates by high-pass filtering the input signal from the photomultiplier to extract the Doppler signal created from particles passing through the fringes in the measurement volume. Internal circuitry then counts a predetermined number of doppler cycles, usually eight, and times them. By knowing the fringe spacing, determined from the geometry of the optics and the laser wavelength, and the time to cross the fringes, measured by the counter, the velocity of an individual particle is obtained.

To link the counter with the HP 21MX computer, an interface (TSI model 1998) is being added. This interface operates with DMA (direct memory access) into the computer to maximize the acceptable data rate. When the counter validates a velocity measurement, it sends it to the TSI interface. This interface then notifies the computer that data is available and suppresses the counter from updating with new velocity information. When ready, the computer fetches the data from the

interface. When the transfer is complete, the interface releases the counter to make the next measurement. The interface itself has a timer and can measure the time between validated velocity measurements. This additional information can be transferred to the computer in the DMA cycles.

After a specified number of data points has been taken, the computer will write the data to the magnetic tape for storage. On-line data analysis will then calculate the sample mean velocity, turbulence intensity, and velocity probability density function. These quantities will then be output to a video monitor. If they correspond to realistic values, the data will be kept. This technique of on-line data analysis allows instant feedback on whether the system is adjusted properly. This technique has been used by other LDV researchers [3.1,3.2] and has successfully indicated such things as improper optical alignment, filter settings, and gain settings in the LDV system.

During this contract reporting period, the TSI interface, the connecting cables, and the appropriate I/O interface card for the HP 21MX have been obtained. The installation of this hardware is nearly complete. Figure 3.1 shows a schematic of the data acquisition system. Preliminary computer programs that control the data acquisition and do the on-line data analysis have been written and await the completion of the hardware link for testing.

During the MHD tests of 1980, it was determined that the color filter provided with the LDV optical system was inadequate to filter the intense radiation of the potassium seed. A special color filter was designed for the system. The filter has been obtained and a special mount is currently being constructed to fit it into the optical train.

One of the difficulties of measuring turbulence suppression in a combustion plasma is the presence of nonturbulent, low frequency fluctuations. Combustion instabilities, fuel, or air feed rate fluctuations will add nonuniformities to the flow that will appear as fluctuations about the mean. These nonuniformities, however, may not have shear generated, dissipative scale eddies, and cannot be called true

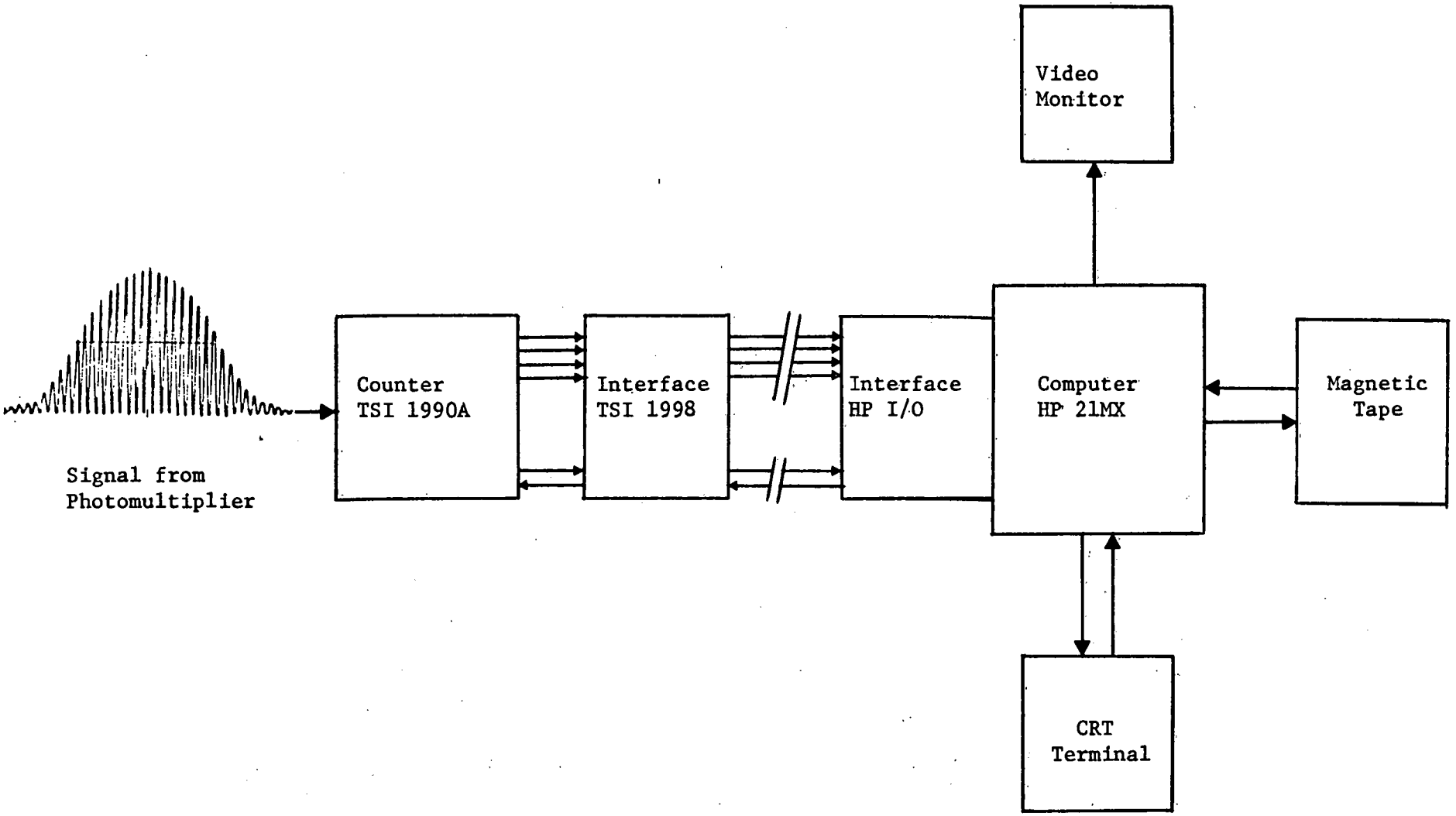

Figure 3.1 LDV data acquisition system.

turbulence. In fact, the length scales of some of these fluctuations will probably exceed the active magnet length. The effect of the magnetic field on such nonuniformities will, in all probability, be quite different than that on dissipative scale turbulence.

To separate these types of disturbances, a power spectrum of the flow will be obtained and filtered. The filter point will be determined from estimates of the lowest frequency components of the turbulence. This can be found by using the characteristic length and velocity of the flow, i.e. the boundary layer thickness and mean velocity. By using the velocity and time information provided by the TSI 1998 interface for each particle, an autocorrelation function can be constructed. The power spectrum is then obtained by taking its Fourier transform. The algorithms to be used have been identified, and preliminary computer programs for this post-test analysis have been written but have not yet been tested. These algorithms will be discussed in future reports.

3.2 Biasing in LDV Measurements

In addition to the work described above, an analysis was made of the biases and uncertainties that are unique to LDV systems. The first bias to be considered is based upon the fact that LDV measures the velocities of particles suspended in a fluid and not the velocity of the fluid itself. As the fluid accelerates, the particles experience a combination of pressure and viscous forces that accelerate the particle toward the fluid velocity. The characteristic response time and, hence, the characteristic frequency of such a particle is a function of the fluid viscosity, the particle size and the particle density. By comparing this particle frequency with the characteristic frequencies of interest in the flow, an estimate of the magnitude of particle slippage can be made. For the flows considered at Stanford, the particle response frequency was two orders of magnitude greater than the characteristic frequency of the flows. It was concluded that particle slip can be ignored.

Another type of biasing arises in LDV applications when there is a correlation between the particle arrival rate and the instantaneous velocity. This biasing, first identified by McLaughlin and Tiederman [3.3], has been termed 1/v biasing. It arises when particles are randomly distributed in the fluid volume. When the fluid velocity is higher than average, a higher than average number of particles pass through the measurement volume, weighting the sample mean toward the higher velocities. In an MHD plasma, however, the particles are randomly distributed in the fluid mass, but not in the fluid volume. Thus, fluid density variations can also play a role. The higher velocity elements of fluid generally have a higher temperature and hence a lower density. This results from the effect of boundary layers cooling fluid elements as they slow them. With particles being distributed according to fluid mass (density), a lower than average volumetric number density of particles is present in high velocity fluid elements. The biasing effect due to fluid density acts in opposition to that of 1/v biasing, reducing the overall bias of the sample mean. For the cases considered in the Stanford MHD plasma, the net biasing effect was found to be small, and will be neglected.

In the literature, there have been a number of other biasing and uncertainty sources proposed. For an LDV system that includes frequency shifting, some particles may be counted twice if their residence time in the measurement volume is long. For the Stanford flows, the residence time is shorter than the counter reset time, so this mode of biasing does not exist. Since larger particles scatter more light, it has been proposed that the LDV samples can be weighted toward the large particle velocity. As long as these larger particles are randomly distributed and do not slip, there is no biasing. This is the case in the Stanford channels.

4.0 HALL FIELD BREAKDOWN

A major problem area in the design of MHD generators is the prevention of axial field breakdown. There are two distinct breakdown modes first observed by Unkel [4.1] in segmented channels; insulator-initiated breakdown and plasma-initiated breakdown. The former arises from internal Joule heating within the interelectrode insulator leading to thermal-electrical breakdown of the insulator. Plasma-initiated breakdown manifests itself as an arc through the plasma adjacent to the interelectrode insulator. The high wall heat flux resulting from the plasma arc often induces insulator breakdown in the adjacent insulator.

To maximize the sustainable axial fields in MHD generators, the processes leading to both plasma and insulator-initiated breakdown and the dependence of the breakdown fields on system parameters must be understood. A computer program has been developed which models the behavior of the interelectrode plasma and insulator regions in the presence of an induced axial field. The program consists of a two-dimensional boundary layer program [4.2,4.3], coupled to a quasi two-dimensional finite-element plasma electrical model developed by Oliver [4.4], both of which can be coupled to either a one-dimensional or a quasi two-dimensional insulator model. The program predicts the onset of insulator-initiated breakdown and can be used to predict the onset of plasma-initiated breakdown.

In the following sections, the computer model and results are discussed and comparisons with available experimental data are made. Figure 4.1 gives a description of the geometry and nomenclature employed in the calculations.

4.1 Theoretical Modelling

For clarity, the theoretical model has been divided into four segments; the plasma dynamics, the electron dynamics, the plasma electrical model, and the insulator thermal-electrical model. Each of these segments will be described below.

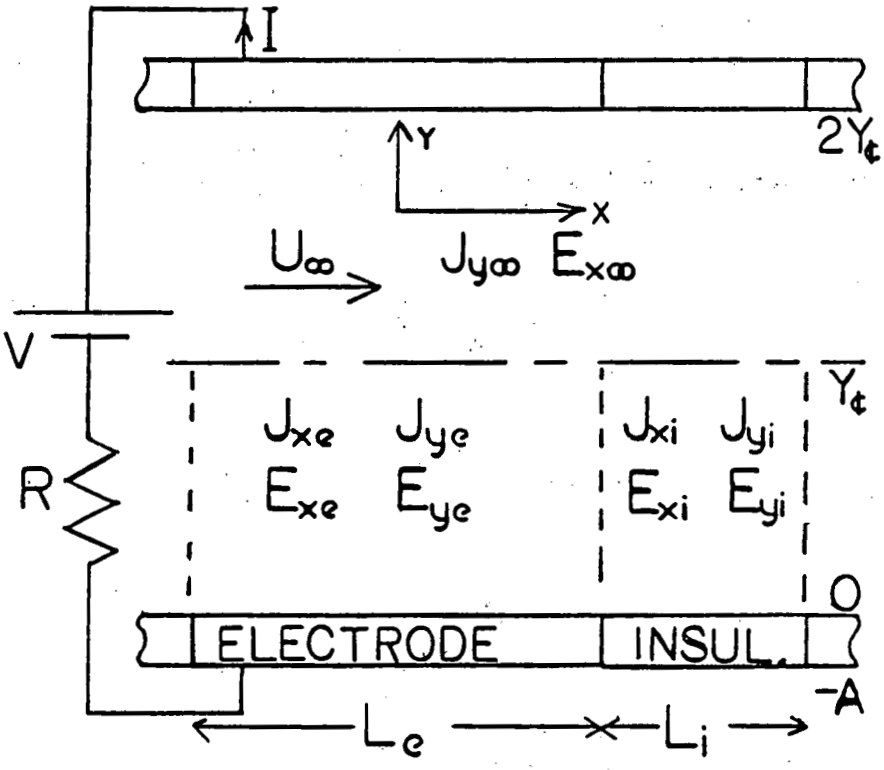

Figure 4.1 Generator configuration used in computer program.

4.1.1 Plasma Dynamics

An existing two-dimensional boundary layer program was utilized to model the plasma dynamics. The model includes the bulk plasma continuity, axial momentum and energy equations as listed below.

Continuity:
$$\frac{\partial \overline{\rho u}}{\partial x} + \frac{\partial \overline{\rho v}}{\partial y} = 0 \tag{4.1}$$

Axial Momentum:
$$\overline{\rho u}\,\frac{\partial \bar{u}}{\partial x} + \overline{\rho v}\,\frac{\partial \bar{u}}{\partial y} = \frac{\partial}{\partial y}\left[(\mu+\rho\varepsilon_m)\frac{\partial \bar{u}}{\partial y}\right] - \frac{\partial p}{\partial x} + J_y B_z \tag{4.2}$$

Energy:
$$\overline{\rho u}\,\frac{\partial \bar{H}}{\partial x} + \overline{\rho v}\,\frac{\partial \bar{H}}{\partial y} = \frac{\partial}{\partial y}\left[\left(\frac{\mu}{Pr} + \rho\varepsilon_D\right)\frac{\partial \bar{H}}{\partial y}\right]$$
$$+ \frac{1}{2}\frac{\partial}{\partial y}\left[(\mu+\rho\varepsilon_m)\left(1 - \frac{1}{Pr}\right)\frac{\partial \bar{u}^2}{\partial y}\right] + \frac{J^2}{\sigma} + J_y \bar{u} B_z \tag{4.3}$$

where
$$\bar{H} \equiv \bar{h} + \frac{\bar{u}^2}{2} . \tag{4.4}$$

In the viscous dissipation term of the energy equation, the turbulent Prandtl number is assumed equal to the molecular Prandtl number.

A transverse pressure model has also been incorporatd to isolate anode-cathode wall differences. The model consists of a solution to the equation

$$\partial p/\partial y = - J_x B_z \tag{4.5}$$

The numerical algorithm utilizes axial damping to reduce the axial pressure gradient imposed by this model at electrode-insulator junctions.

The core boundary conditions for these equations are obtained from a separate core plasma solution [4.3]. The continuity, axial momentum and energy equations are solved in addition to the equation of state for

the plasma. A constraint equation which can restrain any of the core dependent variables is included to provide a total of five core equations for the five dependent variables, axial velocity, enthalpy, pressure, density and channel cross-sectional area.

The wall boundary conditions for the axial momentum and energy equations are the usual no-slip velocity, and continuous temperature and heat flux, respectively. The continuity equation is automatically satisfied by employing the Von Mises transformation.

4.1.2 Electron Dynamics

The program solves the electron continuity equation as presented below [4.2,4.3]

$$\bar{\rho u}\,\frac{\partial \overline{C_e}}{\partial x} + \bar{\rho v}\,\frac{\partial \overline{C_e}}{\partial y} = \frac{\partial}{\partial y}\left[\rho\,(D_a+\varepsilon_D)\frac{\partial \overline{C_e}}{\partial y}\right] + \dot{R}_e \qquad (4.6)$$

The equation consists of a balance between convection, diffusion and an electron source-recombination term. The boundary conditions consist of the equilibrium electron concentration in the core, and a sheath model [4.2] at the channel wall.

The electron energy nonequilibrium is modelled by the equation [4.5]

$$\underset{\sim}{J} \cdot \underset{\sim}{E}' = \frac{2m_e}{m_H}\,\delta_s\,\bar{\nu}_{eH}\,n_e\,\frac{3}{2}k\,(T_e - T). \qquad (4.7)$$

This equation consists of a balance between Joule heating and electron collisional losses through both elastic and inelastic collisions.

4.1.3 Plasma Electrical Model

The plasma electrical model consists primarily of Oliver's finite element model [4.4]. The model assumes two distinct regions, an electrode region and an insulator region. The axial field and transverse current density in each region are given by the following set of equations.

Insulator region

$$J_{yi}(y) = J_{y\infty}\phi(y) \tag{4.8}$$

$$E_{xi}(y) = E_{x\infty}[\phi(y) + (1 + L_e/L_i)(1 - \phi(y))] \tag{4.9}$$

Electrode region

$$J_{ye}(y) = J_{y\infty}\,[\phi(y) + (1 + L_i/L_e)(1 - \phi(y))] \tag{4.10}$$

$$E_{xe}(y) = E_{x\infty}\phi(y) \tag{4.11}$$

Here $\phi(y)$ is a matching function which varies linearly from zero at the wall to unity at the edge of the δ_{99} boundary layer. In practice, these equations have a weak axial dependence due to the axial variation of δ_{99} and the consequent axial variation of ϕ.

The axial current density and transverse electric field in both the electrode and insulator regions are given by the Ohm's law.

$$J_x = \sigma E_x - \beta J_y \tag{4.12}$$

$$E_y = u\,B_z + \frac{1+\beta^2}{\sigma} J_y - \beta E_x \tag{4.13}$$

In addition to these algebraic equations, two additional equations are required to determine $J_{y\infty}$ and $E_{x\infty}$. The two conditions which are enforced are the following:

Zero net hall current over the insulator

$$\int_{-A}^{Y_{\mathfrak{L}}} J_{xi}\, dy = 0 \tag{4.14}$$

Faraday voltage

$$V + IR = -\int_{o}^{2Y_{\ell}} E_{ye}\, dy \tag{4.15}$$

These two integral constraints uniquely determine $J_{y\infty}$ and $E_{x\infty}$.

4.1.4 One-Dimensional Insulator Model

The one-dimensional insulator model assumes that all the properties vary only in the direction normal to the surface. The incident heat flux to the insulator from the plasma is taken as the axial average of the local plasma heat flux to the insulator surface. The axial current density in the insulator is given by

$$J_x = \sigma E_x \tag{4.16}$$

The insulator energy equation is solved to determine $T(y)$ and therefore $\sigma(y)$. Thus

$$\frac{d}{dy}\left(K(T)\,\frac{dT}{dy}\right) + \sigma(T)\,E_x^2 = 0 \tag{4.17}$$

where the electrical conductivity, $\sigma(T)$, and the thermal conductivity, $K(T)$ are expressed by algebraic relations of the form

$$\sigma(T) = \sigma_o \exp(-A/T) \tag{4.18}$$

$$K(T) = \sum_{i=o}^{N} k_i\, T^i \tag{4.19}$$

The boundary conditions on the problem enforce continuous heat flux and temperature at the plasma-insulator interface. A heat transfer coefficient and coolant temperature are specified at the cooled wall.

4.1.5 Two-Dimensional Insulator Model

The two-dimensional insulator model consists of a two-dimensional energy equation coupled to a quasi two-dimensional insulator electrical model. The exact electrical boundary conditions for the insulator require that the tangential electric field be continuous at the boundaries. Due to the high electrical conductivity of the adjacent electrodes, it is expected that the transverse electric field at the insulator-electrode boundary will be insignificant relative to the axial electric field at the insulator-plasma boundary. The electrical model therefore assumes that the insulator transverse current density is negligible throughout the insulator.

$$J_y = 0 \tag{4.20}$$

The current conservation equation then reduces to the form

$$\frac{\partial J_x}{\partial x} = 0 \tag{4.21}$$

Equation (4.21) requires that the axial current density be of the form $J_x(y)$. Ohm's law reduces to

$$E_x(x,y) = \frac{J_x(y)}{\sigma(T)} \tag{4.22}$$

The insulator axial field is constrained by the equation

$$-\int_o^{L_i} E_x(x,y)\, dx = V_x \tag{4.23}$$

where V_x, the axial gap voltage, is obtained from the plasma solution. By combining Eqs. (4.22) and (4.23) we obtain

$$J_x(y) = \frac{-V_x}{\int_o^{L_i} \frac{dx}{\sigma(T)}} \tag{4.24}$$

The two-dimensional insulator energy equation is given by

$$\frac{\partial}{\partial x}\left(K(T)\,\frac{\partial T(x,y)}{\partial x}\right) + \frac{\partial}{\partial y}\left(K(T)\,\frac{\partial T(x,y)}{\partial y}\right) + \sigma(T)\,E_x^2\,(x,y) = 0 \tag{4.25}$$

where $K(T)$ and $\sigma(T)$ are given by the algebraic equation described in the previous section. The Joule heating term in Eq. (4.25) can be reduced to the following form by employing Eqs. (4.22) and (4.24):

$$\sigma(T)\,E_x^2\,(x,y) = \frac{J_x^2(x,y)}{\sigma(T)} = \frac{V_x^2}{\sigma(T)\left[\int_o^{L_i} \frac{dx}{\sigma(T)}\right]^2} \tag{4.26}$$

The boundary conditions for the insulator energy equation are

- continuous temperature and heat flux at the plasma insulator interface
- $u_e(T(o,y) - T_e(y)) = K\,\frac{\partial T}{\partial x}\,(o,y)$
- $u_e(T(L_i,y) - T_e(y)) = -K\,\frac{\partial T}{\partial x}\,(L_i,y)$ (4.27)
- $u_B(T(x,-A) - T_c(x)) = K\,\frac{\partial T}{\partial y}\,(x,-A)$

where u_e and u_B are specified heat transfer coefficients, $T_e(y)$ is the electrode transverse temperature distribution, and $T_c(x)$ is a specified cooled wall temperature distribution.

The energy equation is solved numerically by the method of successive overrelaxation. Between successive iterations on the temperature, the insulator electrical conductivity, the insulator thermal conductivity and the electrical solution are updated.

Computation Procedure. The program reaches convergence via iteration. It marches axially along electrode-insulator pairs. At the end of each pair, $J_{y\infty}$, $E_{x\infty}$, and the insulator solution are recalculated, a new iteration is then initiated.

At the end of each iteration, the condition $dq_{surf}/dT_{surf} < q_{surf}/(T_{surf}-T_{\infty})$ is checked for the insulator. If this condition is satisifed, further increases in the insulator surface temperature will induce a greater surface heat flux than can be removed by the insulator. This corresponds to thermal instability of the insulator, that is insulator initiated breakdown.

Plasma initiated breakdown is given by the condition $dV_x/dJ_y \leq 0$. If between two consecutive computer runs, the interelectrode voltage remains unchanged or decreases, with a corresponding increase in the calculated core current density, then plasma initiated breakdown has occurred.

4.2 Theoretical Results

Computer cases have been run to study the dependence of the interelectrode breakdown voltage on system parameters such as electrode wall component scales, transverse electrode current density and its corresponding boundary layer Joule heating, and anode-cathode wall differences. In addition, several mechanisms affecting the behavior of the interelectrode region have been observed. These mechanisms will be described below.

Anode-cathode wall differences can be attributed to the transverse pressure distribution induced by the interaction of the axial current with the magnetic field. Lower plasma pressures occur at the anode wall. This raises the plasma conductivity which increases the axial current leakage and thereby reduces the induced axial voltage for a given transverse current density. This leads to lower breakdown voltages for the anode wall as compared to the cathode wall.

Four Joule heating mechanisms which enhance insulator breakdown have been observed. The internal Joule heating within the insulator increases the insulator temperature and reduces the ability of the insulator to remove the incident plasma heat flux. The Joule heating in the upstream electrode boundary layer heats the plasma boundary layer and increases the plasma heat flux to the downstream insulator. The plasma

Joule heating in the electrode boundary layer also raises the electrode surface temperature which results in reduced axial thermal conduction losses from the insulator to the adjacent electrodes. Finally, plasma Joule heating due to axial leakage in the insulator boundary layer increases the plasma heat flux to the insulator. The latter mechanism is of secondary importance to insulator heat flux and insulator initiated breakdown, however, it is of primary importance to plasma initiated breakdown.

Two mechanisms which enhance the sustainable insulator electric field have been observed. Due to the lower average surface temperature of the electrodes relative to the interelectrode insulators in this study, the boundary layer leaving the electrode region and entering the insulator region requires a finite length to thermally equilibrate. This reduces the heat flux to the insulator leading edge which results in improved electrical performance for the insulator. This effect becomes more predominant as the insulator width is reduced. With the two-dimensional insulator thermal-electrical model, improved insulator cooling by way of axial-thermal conduction to neighboring electrodes increases the insulator sustainable electric field as the insulator width is reduced.

The results of this study have clarified the dependence of the breakdown mode on system parameters. Insulator initiated breakdown becomes the predominant breakdown mechanism as the thermal loading of the insulator is increased. As the thermal loading is decreased by such mechanisms as reduced upstream electrode current density or reduced insulator width, plasma initiated breakdown becomes predominant.

The computer results which are presented below fall into five categories. In the first four categories, the electron energy equation was not used. These categories are listed below.

- 1-D insulator model with constant L_e/L_i
- 1-D insulator model with constant 3.8 cm electrode pitch
- 2-D insulator model with constant L_e/L_i
- 2-D insulator model with constant 3.8 cm electrode pitch.

The fifth category consists of two computer cases, one without the electron energy equation, and one with the electron energy equation included. These results are compared with existing experimental data taken by Unkel [4.1] under similar flow conditions.

For the first four categories, a constant core pressure constraint is enforced. For the fifth category, a constant channel area constraint is enforced so as to match the experimental conditions as closely as possible. Table 4.1 contains the values of the system parameters which were used for all the computer cases.

Figures 4.2 through 4.5 contain the results for the one-dimensional insulator model with constant L_e/L_i. Figure 4.2 contains the load lines for three different electrode wall scales. In each case one observes insulator initiated breakdown. Figure 4.3 contains the breakdown voltages and electric fields for the three cases. One can observe that the breakdown voltage decreases as the insulator width is reduced. However, the core and surface breakdown electric fields increase by 30% as the insulator width is reduced from 0.8 cm to 0.2 cm. This can be attributed to the finite boundary layer equilibration length. Figure 4.4 indicates that the insulator surface temperature rises as the electrical loading increases. This can be attributed to the four Joule heating mechanisms described previously. The primary mechanisms are internal insulator Joule heating and Joule heating in the upstream electrode boundary layer. One can also observe that the insulator surface temperature decreases as the insulator width is reduced. This can be attributed to the increasing significance of the boundary layer equilibration length as the insulator width is reduced. Figure 4.5 indicates that the insulator surface heat flux decreases as insulator width is reduced, again attributable to the boundary layer equilibration length. One can also observe that increasing the electrical loading leads to a peak in the insulator heat flux due to the increasing importance of the internal insulator Joule heating.

Figures 4.6 through 4.9 contain results for the one-dimensional insulator model with a constant 3.8 cm electrode pitch. As with Fig. 4.2,

Table 4.1

System Conditions for Computer Cases

U_∞ = 450 m/sec

T_∞ = 2725 K

p_∞ = 1 atm

σ_∞ = 10.6 mhos/m

B = 2.7 T

N_2/O_2 = 0.5

Distance from Nozzle = 10 cm

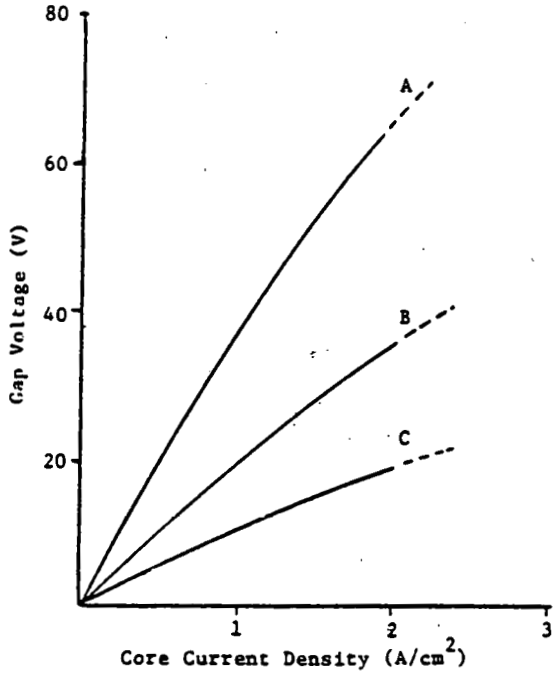

Fig. 4.2 Gap voltage vs. core current density.

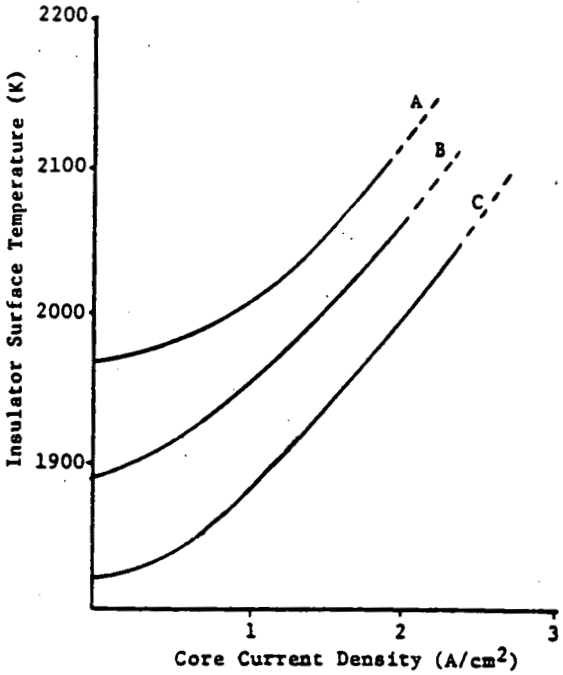

Fig. 4.4 Insulator surface temperature vs. core current density.

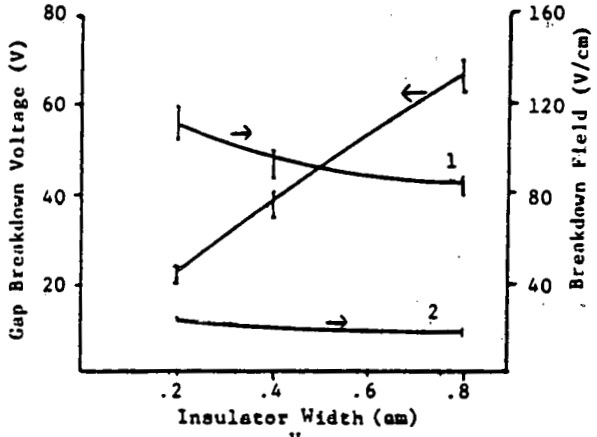

$$1: \quad E_x = \frac{V_{x\ br}}{L_i}$$

$$2: \quad E_x = \frac{V_{x\ br}}{L_i + L_e}$$

Fi 4.3 Breakdown voltages and electric fields vs. insulator width.

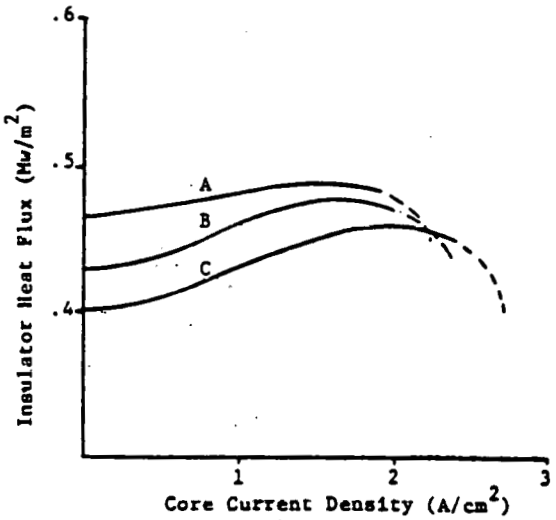

Fig. 4.5 Insulator heat flux vs. core current density.

Computer results for 1-D insulator model with constant L_e/L_i (Figs. 4.2–4.5).

A: L_e = 3.0 cm, L_i = 0.8 cm

B: L_e = 1.5 cm, L_i = 0.4 cm

C: L_e = 0.75 cm, L_i = 0.2 cm

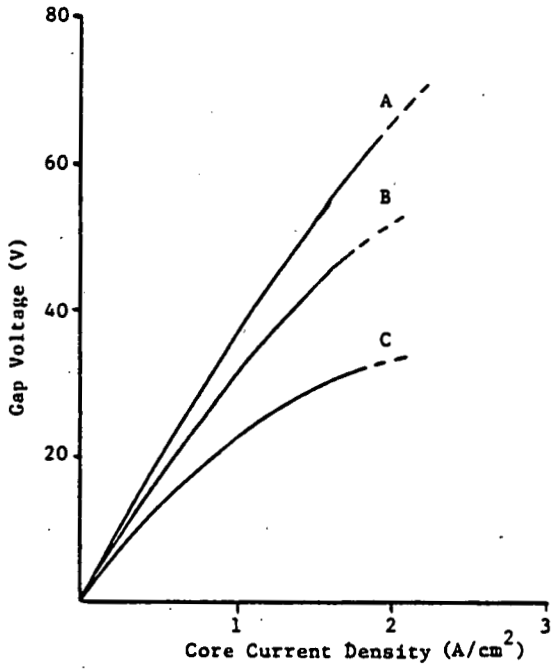

Fig. 4.6 Gap voltage vs. core current density.

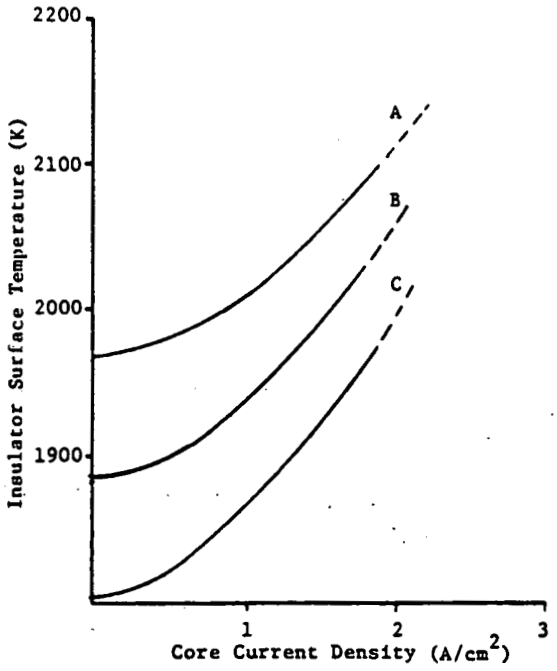

Fig. 4.8 Insulator surface temperature vs. core current density.

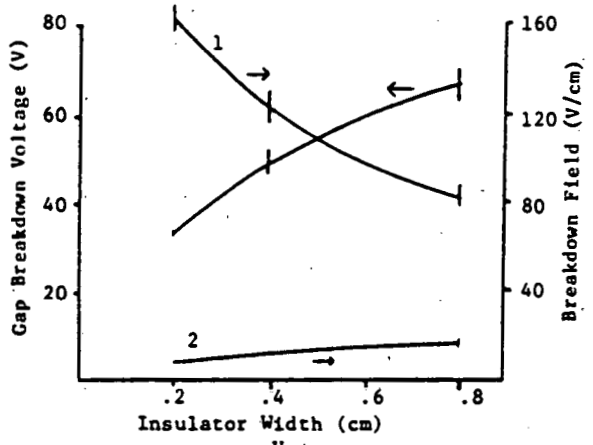

$$1: \quad E_x = \frac{V_x|_{br}}{L_i}$$

$$2: \quad E_x = \frac{V_x|_{br}}{L_i + L_e}$$

Fig. 4.7 Breakdown voltage and electric fields vs. insulator width.

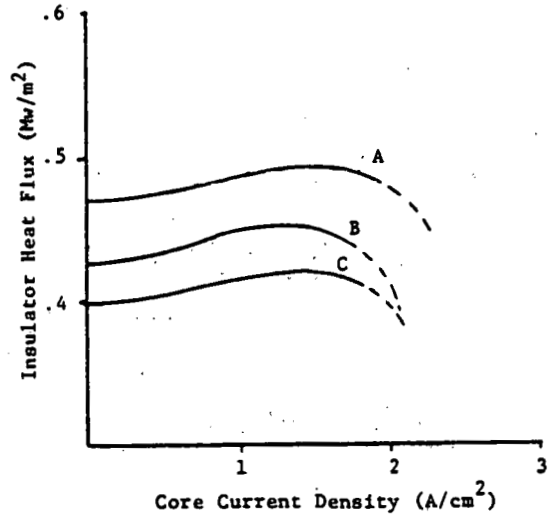

Fig. 4.9 Insulator heat flux vs. core current density.

Computer results for 1-D insulator model with constant 3.8 cm electrode pitch (Figs. 4.6–4.9).

A: L_e = 3.0 cm, L_i = 0.8 cm

B: L_e = 3.4 cm, L_i = 0.4 cm

C: L_e = 3.6 cm, L_i = 0.2 cm

Fig. 4.6 indicates that all three cases undergo insulator initiated breakdown, with the wider insulators sustaining larger axial voltages. Figure 4.7 indicates that the surface breakdown electric field rises by 100% as the insulator width is reduced from 0.8 to 0.2 cm. The improvement over the cases described in Fig. 4.3 can be attributed to lower upstream electrode current densities. Due to enhancement of the insulator surface electric field for a given core field as the ratio of L_e/L_i increases, one can observe reduced core breakdown fields as insulator width is reduced. Figures 4.8 and 4.9 show similar trends to 4.4 and 4.5. Comparison of Figs. 4.5 and 4.9 indicates that for a given insulator size and core current density, the latter cases experience a lower insulator surface heat flux. This can be attributed primarily to the larger insulator axial field and corresponding internal Joule heating for the cases of Fig. 4.9.

Figures 4.10 through 4.13 contain results for the two-dimensional insulator model with constant L_e/L_i. Figure 4.10 indicates reductions in the breakdown voltage as insulator width is reduced. However, one should note the increase in the breakdown transverse current density as insulator width is reduced. Figure 4.10 also indicates that slightly higher breakdown voltages can be attained on the cathode wall. Figure 4.11 indicates that the surface and core breakdown electric fields increase by more than 100% as the insulator width is reduced from 0.8 to 0.2 cm. This can be compared to the 30% improvement of Fig. 4.3. The improvement in insulator performance for the cases in Fig. 4.11 can be attributed to the finite boundary layer equilibration length, like the cases of Fig. 4.3, and also to the increasing axial thermal conduction losses from the insulator to the adjacent electrodes as the insulator width is reduced. The improved performance for the cases in Fig. 4.11 compared to those of Fig. 4.3, indicates that axial thermal conduction is more significant than the boundary layer equilibration length. The trends in Fig. 4.12 are similar to the trends in Figs. 4.4 and 4.8, except that one can observe larger reductions in the insulator surface temperature as insulator width is reduced. This is attributable to axial thermal conduction losses to the neighboring electrodes. Figure

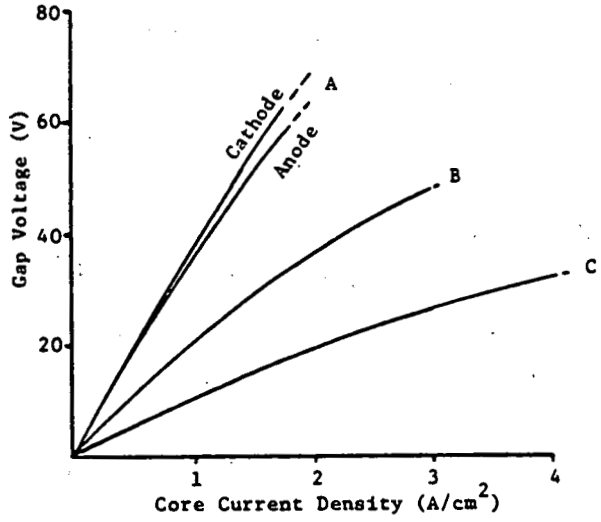

Fig. 4.10 Gap voltage vs. core current density.

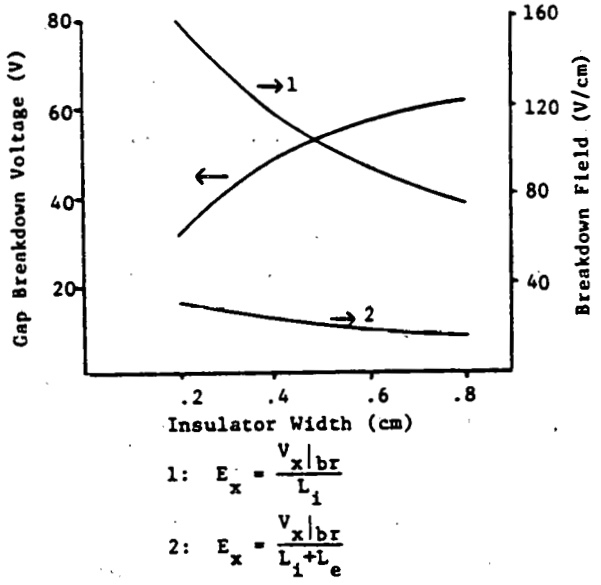

$$1: \quad E_x = \frac{V_x|_{br}}{L_i}$$

$$2: \quad E_x = \frac{V_x|_{br}}{L_i + L_e}$$

Fig. 4.11 Breakdown voltages and electric fields vs. insulator width.

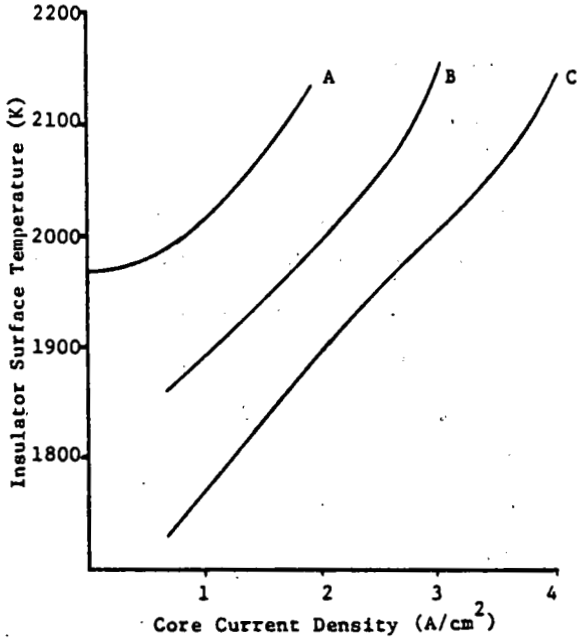

Fig. 4.12 Insulator surface temprature vs. core current density.

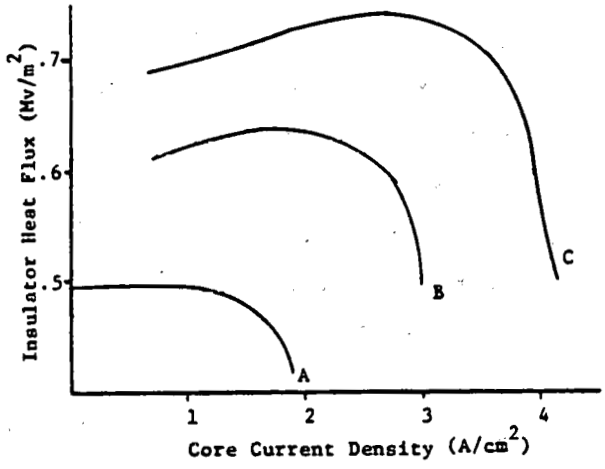

Fig. 4.13 Insulator heat flux vs. core current density.

Computer results for 2-D insulator model with constant L_e/L_i (Figs. 4.10-4.13).

A: L_e = 3.0 cm, L_i = 0.8 cm

B: L_e = 1.5 cm, L_i = 0.4 cm

C: L_e = 0.75 cm, L_i = 0.2 cm

4.12 indicates a surface temperature reduction of 260 K as the insulator width is reduced from 0.8 cm to 0.2 cm. Figure 4.13 indicates, as before, that insulator surface heat flux peaks due to the growing contribution of internal Joule heating as the electrical loading increases. However, Fig. 4.13 also indicates that insulator surface heat flux increases with reductions in insulator width, unlike Figs. 4.5 and 4.9. Axial conduction losses will increase the insulator surface heat flux by reducing its temperature, while the boundary layer equilibration length will reduce the insulator surface heat flux. This observation therefore implies that the contribution of axial thermal conduction is greater than that of the boundary layer equilibration length as insulator width is reduced.

Figures 4.14 through 4.17 contain results for the two-dimensional insulator with a constant 3.8 cm electrode pitch. Figure 4.14 indicates the onset of plasma breakdown. The breakdown mode for the 0.8 cm insulator was insulator initiated breakdown. The breakdown mode for the 0.4 cm insulator could not be determined with certainty since both insulator and plasma initiated breakdown occurred together. The 0.2 cm insulator experienced plasma initiated breakdown. Figure 4.15 indicates that the breakdown voltage decreases with decreasing insulator width, however, one should note the weak dependence of the breakdown voltage on insulator width for the larger insulator widths. This agrees favorably with the experimental results of Zalkind et al. [4.6]. As before, we see large increases in the insulator surface breakdown electric field as insulator width is reduced. Unlike the previous cases, the surface breakdown electric field is concave up as shown in Fig. 4.15. This indicates the onset of plasma breakdown limitations. As the insulator width is reduced, axial cooling of the insulator successfully eliminates insulator initiated breakdown, at which point the plasma breakdown threshold becomes the limitation on gap performance. The trends in Fig. 4.16 agree with those of Fig. 4.12. Additionally, one can observe that the 0.2 cm insulator does not attain the high surface temperatures of the 0.4 cm and 0.8 cm insulators at breakdown. This is to be expected since insulator initiated breakdown was not the breakdown mode for the 0.2 cm

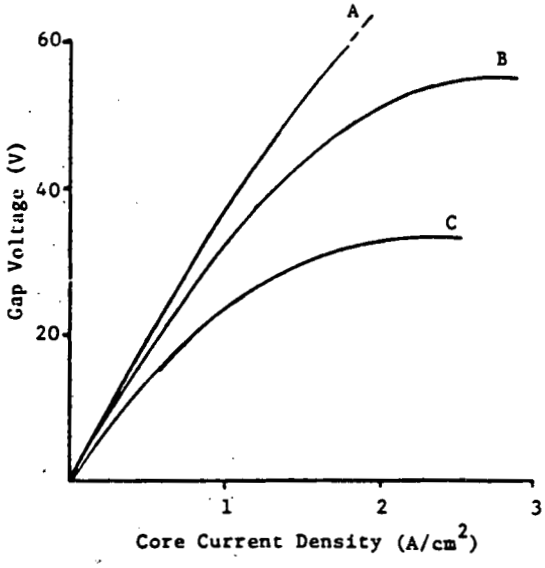

Fig. 4.14 Gap voltage vs. core current density.

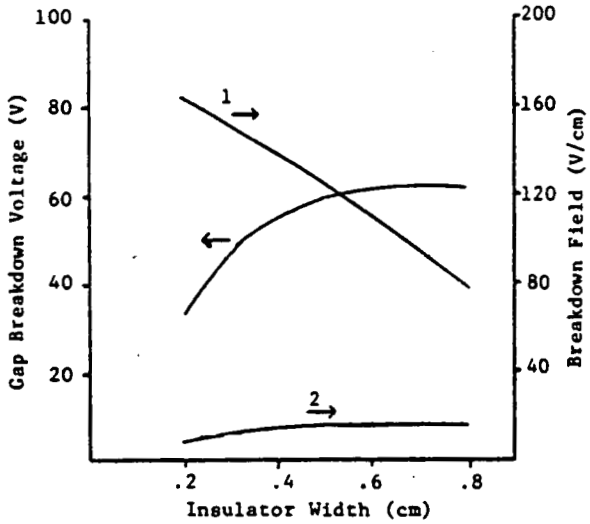

$$1: \quad E_x = \frac{V_{x|br}}{L_i}$$

$$2: \quad E_x = \frac{V_{x|br}}{L_i + L_e}$$

Fig. 4.15 Breakdown voltages and electric fields vs. insulator width.

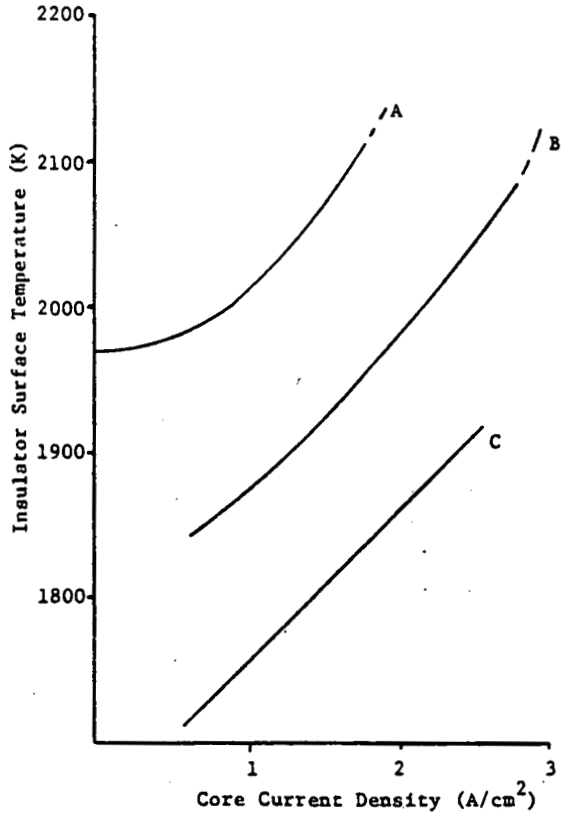

Fig. 4.16 Insulator surface temperature vs. core current density.

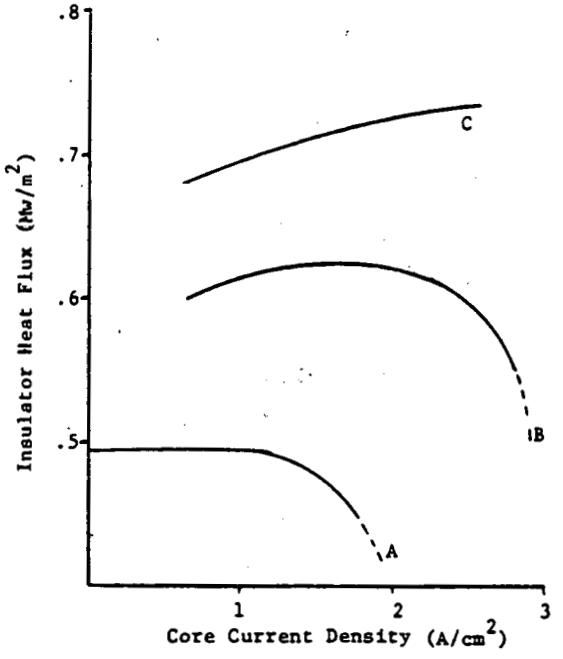

Fig. 4.17 Insulator heat flux vs. core current density.

Computer results for 2-D insulator model with constant 3.8 cm electrode pitch (Figs. 4.14-4.17).

A: L_e = 3.0 cm, L_i = 0.8 cm

B: L_e = 3.4 cm, L_i = 0.4 cm

C: L_e = 3.6 cm, L_i = 0.2 cm

insulator. The trends in Fig. 4.17 agree with those of Fig. 4.13, except for the 0.2 cm insulator case. In the latter case, the internal Joule heating in the insulator stays insignificant. The surface heat flux therefore rises steadily as the electrical loading increases.

Figures 4.18 through 4.20 contain results for the two-dimensional insulator model, with and without the electron energy equation model. The results are also compared with existing experimental data taken by Unkel [4.1] under similar flow conditions. Figure 4.18 indicates that inclusion of the electron energy equation raises the breakdown voltage by approximately 10%. This is due to thermal reasons which will be described shortly. One can also observe the close agreement between both calculated load lines and the existing experimental data. The experimentally observed breakdowns, like the calculated breakdowns, were insulator initiated. Examination of Fig. 4.19 indicates a reduction in the insulator surface temperature by inclusion of the electron energy equation model. Examination of Fig. 4.20 indicates that with the electron energy equation model, the inulator can dissipate a higher heat flux. The differences in these results can be attributed primarily to the Joule heating in the upstream electrode boundary layer. Inclusion of the electron energy equation reduces upstream Joule heating due to the higher plasma electrical conductivity in the electrode boundary layer. This reduces the Joule heating dependent heat flux to the insulator. In addition, it lowers the electrode surface temperature and thereby improves axial insulator cooling. These mechanisms reduce the insulator surface temperature which in turn reduces the internal Joule heating for a given axial voltage. This further improves the ability of the insulator to dissipate the incident heat flux. The combined effect of these mechanisms is to reduce the insulator surface temperature and increase the surface heat flux for a given axial voltage.

Figures 4.21 and 4.22 are plots of the gap breakdown voltage vs. upstream electrode current density for the computer cases described above. In general one can observe an increase in the breakdown voltage as upstream electrode current density is reduced. These results agree

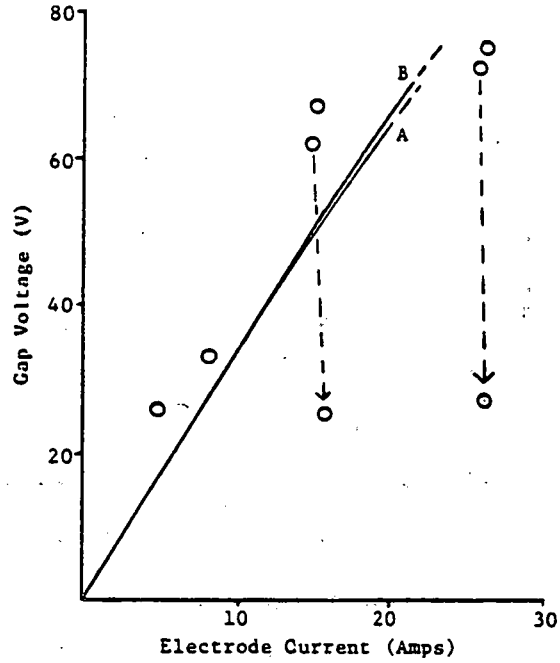

Fig. 4.18 Gap voltage vs. electrode current.

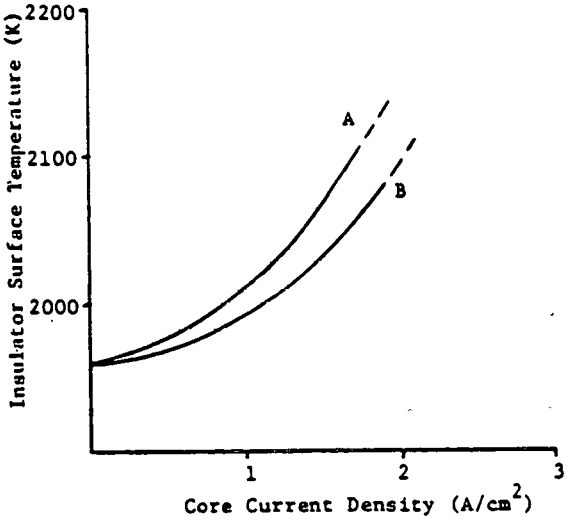

Fig. 4.19 Insulator surface temperature vs. core current density.

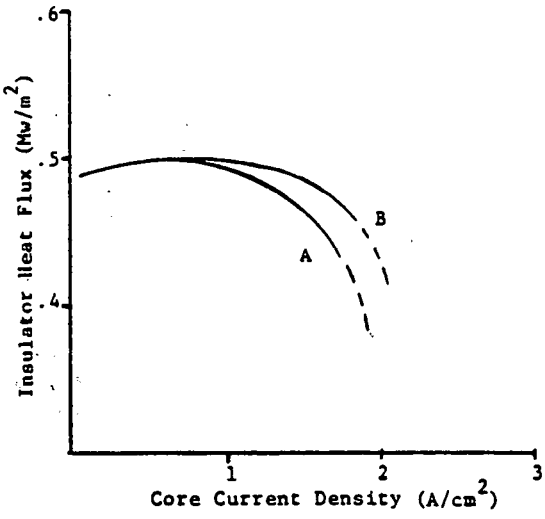

Fig. 4.20 Insulator heat flux vs. core current density.

Comparison of computer results with and without electron energy equation, with experimental results of Unkel. L_e = 3.0 cm, L_i = 0.8 cm: constant channel area constraint (Figs. 4.18-4.20).

A: without electron energy equation
B: with electron energy equation

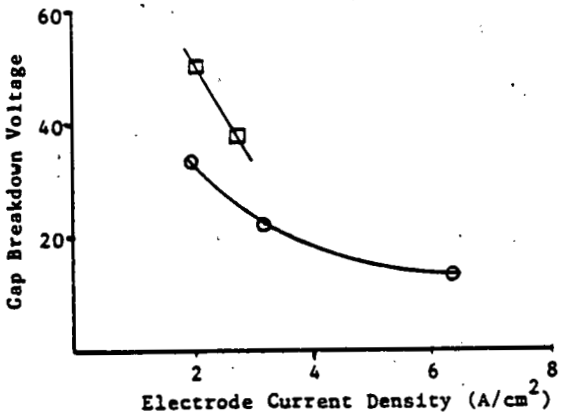

Fig. 4.21 Gap breakdown voltage vs. electrode current density for 1-D insulator model.

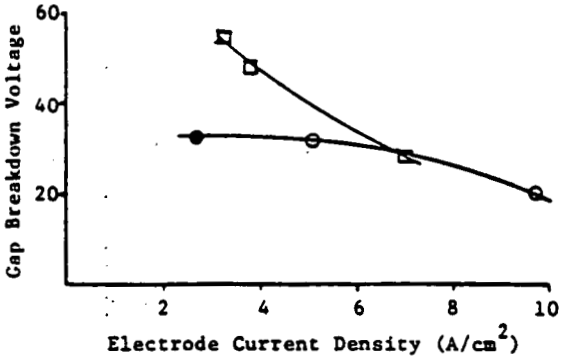

Fig. 4.22 Gap breakdown voltge vs. electrode current density for 2-D insulator model.

Breakdown thresholds for 1-D and 2-D insulator models (Figs. 4.21-4.22).

- ○ 0.2 cm gap, insulator initiated breakdown
- ● 0.2 cm gap, plasma initiated breakdown
- □ 0.4 cm gap, insulator initiated breakdown

favorably with the experimental results of Zalkind et al [4.6]. Figure 4.22 indicates the onset of plasma initiated breakdown for the 0.2 cm insulator. As the upstream electrode current density is reduced, the insulator initiated breakdown voltage increases and finally the plasma initiated breakdown threshold is exceeded. This results in a weaker dependence of the gap breakdown voltage on electrode current density. This weaker dependence is a result of the different mechanisms which govern plasma initiated breakdown as compared to insulator initiated breakdown. The primary mechanism for the former breakdown mode is Joule heating in the insulator boundary layer due to axial leakage. The axial leakage is primarily dependent on the gap voltage and not the transverse current density.

4.3 Conclusions

A two-dimensional MHD computer code has been developed which predicts the onset of insulator and plasma initiated breakdown. The results from the code demonstrate the importance of an insulator model for accurate predictions of the behavior of the interelectrode region.

The code has been used to study the dependence of the interelectrode breakdown voltage on system parameters such as insulator width, electrode current density and magnetic field direction. In addition, several mechanisms which enhance insulator initiated breakdown have been observed. The onset of plasma initiated breakdown has also been predicted. There is good agreement between the computed results and the experimental results of Unkel [4.1]; in addition the trends predicted by the computer results agree favorably with the experimental results of Zalkind et al [4.6].

5.0 DISK GENERATOR STUDIES

During the present reporting period, progress has been made mainly in two areas; analytical and numerical calculations of fluid and electrical behavior, and studies of performance prediction. In the analytical and numerical work, current discharge phenomena in large, high interaction disk generators were studied. In the performance prediction area, calculations of the performance of baseload inflow disk generators were performed and were compared with linear generators.

5.1 Current Distribution and Nonuniformities

Current distribution and nonuniformity effects in the r-θ plane of large, baseload-size disk generators have been investigated using the finite element computer codes. Description of the finite element codes and some of the preliminary results have been given in previous progress reports [5.1,5.2]. For the sake of completeness, however, salient features of the finite element methods employed are briefly reviewed below, prior to the presentation of the results.

For high MHD interaction as might be expected for baseload size MHD disk generators, the fluid dynamic and electrical equations need to be solved together. The appropriate equations, assuming axial uniformity ($\partial/\partial z = 0$), are

Continuity Equation:

$$\frac{1}{rz}\frac{\partial}{\partial r}(\rho v_r rz) + \frac{1}{r}\frac{\partial}{\partial \theta}(\rho v_\theta) = 0$$

Momentum Equations:

$$\rho v_r \frac{\partial v_r}{\partial r} + \frac{\rho v_\theta}{r}\frac{\partial v_r}{\partial \theta} - \frac{\rho v_\theta^2}{r} = -\frac{\partial P}{\partial r} + j_\theta B$$

$$\rho v_r \frac{\partial v_\theta}{\partial r} + \frac{\rho v_\theta}{r}\frac{\partial v_\theta}{\partial \theta} + \frac{\rho v_r v_\theta}{r} = -\frac{1}{r}\frac{\partial P}{\partial \theta} - j_r B$$

Energy Equation:

$$\rho v_r \frac{\partial h_{tot}}{\partial r} + \frac{\rho v_\theta}{r} \frac{\partial h_{tot}}{\partial \theta} - \left[\frac{1}{rz} \frac{\partial}{\partial r} (q_r rz) + \frac{1}{r} \frac{\partial}{\partial \theta} (q_\theta)\right]$$

$$- (j_r E_r + j_\theta E_\theta) = 0$$

Electrical Potential Equation:

$$\frac{1}{rz} \frac{\partial}{\partial r} \left[\frac{\sigma}{1+\beta^2} \left(- \frac{\partial \phi}{\partial r} + \frac{\beta}{r} \frac{\partial \phi}{\partial \theta} + Bv_\theta + \beta B v_r\right) rz\right]$$

$$+ \frac{1}{r} \frac{\partial}{\partial \theta} \left[\frac{\sigma}{1+\beta^2} \left(- \frac{1}{r} \frac{\partial \phi}{\partial \theta} - \beta \frac{\partial \phi}{\partial r} + \beta B v_\theta - B v_r\right)\right] = 0$$

where the electric potential ϕ is defined as

$$E_r = - \frac{\partial \phi}{\partial r} \qquad E_\theta = - \frac{1}{r} \frac{\partial \phi}{\partial \theta}$$

and the currents are related by Ohm's Law

$$j_r = \frac{\sigma}{1+\beta^2} \left[E_r - \beta E_\theta + B \left(v_\theta + \beta v_r\right)\right]$$

$$j_\theta = \frac{\sigma}{1 + \beta^2} \left[E_\theta + \beta E_r + B \left(\beta v_\theta - v_r\right)\right] .$$

The channel height z is prescribed as a specific function of radius.

Instead of coupling the fluid and electrical equations step-wise as has been done in the previous work, it was decided to attempt a simultaneous solution of the equations using a Finite Element Method (FEM). Plasma properties required by the equations are determined at each point using a curve fit routine for either alcohol or Montana Rosebud coal combustion products seeded with potassium. The code was initially developed for a small scale disk and once working satisfactorily was expanded for larger size disks. In cases studied to date, the static pressures and temperatures have been in the ranges expected for baseload

disks. The channels studied are constant Mach number channels with M = .8. This was picked to avoid a Mach number of unity where the numerical calculations break down. An inlet swirl of unity and an inlet load factor of 0.45 were chosen as representative for disk operating conditions. The size of the computer available limits the overall number of elements that can be used. A 1/12 section of the disk is used with periodic boundary conditions imposed and the length limited by the maximum number of elements.

Two cases are presented, one for an outflow channel with a temperature and velocity deficit in the inlet conditions as might be caused by cooled guide vanes, another for an inflow channel with a linear change in temperature with angular position as might be caused by an inflow inlet scroll. The z contours for these cases are curve fits from a one-dimensional Runge-Kutta calculation for constant Mach number. The inlet conditions for the z contour calculation are given in Table 5.1. The same conditions are used for the no property variation cases to which the cases with property variations are compared.

To simulate effects of cooled guide vanes in an outflow channel, flat-bottomed, V-shaped, in-phase deficits of temperature and velocity were imposed. The width of the deficits was one-quarter of the computational section inlet. The temperaure deficit was a maximum of 1.5% which corresponds to a conductivity deficit of 17.4%, and the velocity deficit was 9.5% with the swirl angle kept constant. The inlet is at a radius of 1.5 m with a height of 20 cm and the channel extends to a radius of 2.255 m where the height is 15.9 cm. The load voltage was kept the same 5150 volts as in the no variation case. The results are summarized in Table 5.2.

To simulate the effects of temperature variations in inflow disks due to the inlet scroll, a linear temperature decrease with angular position at the inlet was used. The temperature decrease was a total of 1.4% and the velocity was uniform across the inlet with a maximum Mach number of 0.8. The inlet of this channel is at a radius of 4 m with a height of 7.4 cm and the plasma flows inward to a radius of 2.81 m where

Table 5.1

INLET CONDITIONS

Total Pressure	6 atm
Total Temperature	2800 K
Mach Number	0.8
Inlet Swirl	1.0
Inlet Load Factor	0.45
Mass Flow	500 kg/sec
Enthalpy Influx	1960 MW

Table 5.2

OUTFLOW RESULTS

Case	Inlet	Maximum % Variation	Outlet	Load Current (Amps)	Load Voltage (Volts)	Enthalpy Influx (MW)	Power Output (MW)	% of Inlet Enthalpy Extracted
No Property Variation		None		20,190	5,150	1,960	104.0	5.31
With Property Variation	1.5 17.4 9.5	Temp Cond Vel	1.1 15.7 13.6	18,250	5,150	1,915	94.0	4.91

the height is 19.1 cm. Again the load voltage was kept the same as for the no variation case, 9500 volts for this channel. The results of this case are summarized in Table 5.3.

Figures 5.1 and 5.2 show the potential distribution in the outflow and inflow channels, respectively for the variation cases. A noticeable effect on the potential distribution occurs in the outflow guide vane case while the change in the potential distribution for the inflow variation case is negligible. The greatest effect on the current distribution is due to the conductivity variation. Figure 5.3 shows the conductivity throughout the channel for the outflow case. The conductivity variation, which follows the temperature variation, changes little in its size or shape as it moves with the plasma flow. Figure 5.4 shows the radial velocity component for the same case. Again the initial variation follows the plasma flow changing little in size or shape, but on one side of the variation there is a noticeable lowering of the radial velocity. This is due to the MHD interaction to the tangential current component which is shown in Fig. 5.5. A similar though smaller effect is observed in the inflow case near the point where the high temperature end of the inlet temperature distribution meets the low end of the previous distribution (Figs. 5.6 and 5.7).

The variations have the overall result of reducing the channel performance. These cases have assumed the channel was designed for no variations. The variation cases were then run assuming the same load voltage. Though the variations reduce the enthalpy influx by 2.3% for the outflow and 2.6% for the inflow, the power output is reduced 9.6% and 10%, respectively, and the percent enthalpy extracted drops 7.5% for the outflow and 7.7% for the inflow. Since the decrease in power output and enthalpy extraction are much larger than the decrease in enthalpy influx, the property variations significantly reduce the channel performance.

These studies will be continued as the effects of property variations are examined for other load conditions and operating parameters. Also an investigation of electrode segmentation and core current

Table 5.3

INFLOW RESULTS

Case	Inlet	Maximum % Variation	Outlet	Load Current (Amps)	Load Voltage (Volts)	Enthalpy Influx (MW)	Power Output (MW)	% of Inlet Enthalpy Extracted
No Property Variation		None		19,840	9,500	1,960	188.5	9.62
With Property Variation	1.4	Temp	1.5	17,850	9,500	1,910	169.6	8.88
	15.8	Cond	13.2					
	0	Vel	2.4					

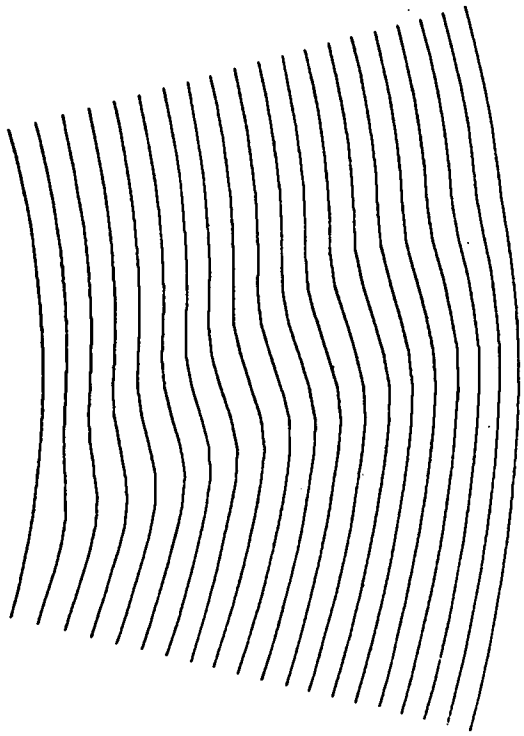

Fig. 5.1 R-θ potential distribution for outflow variation case.

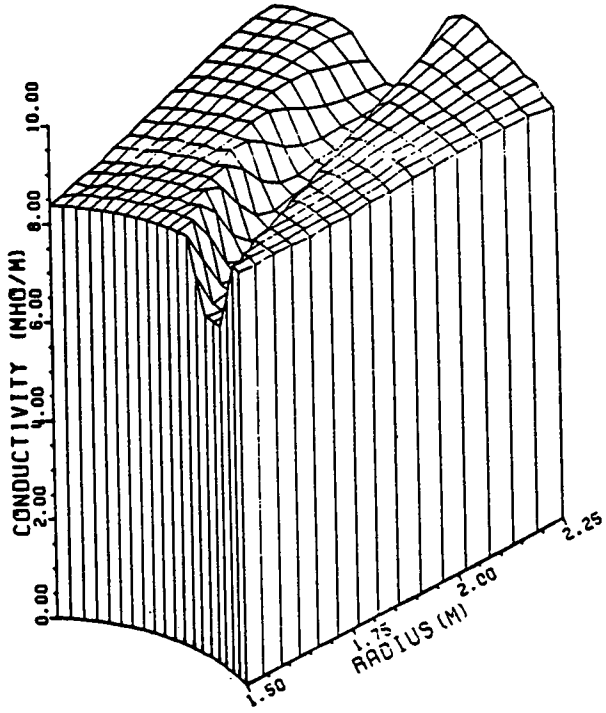

Fig. 5.3 Conductivity in the outflow variation case.

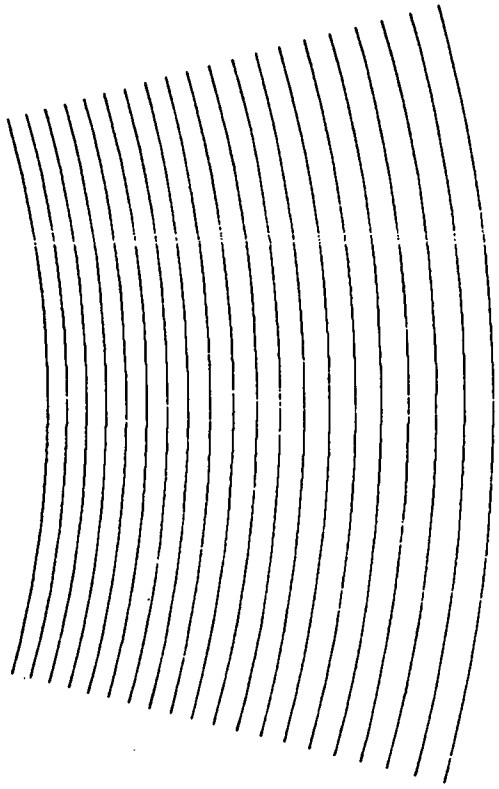

Fig. 5.2 R-θ potential distribution for inflow variation case.

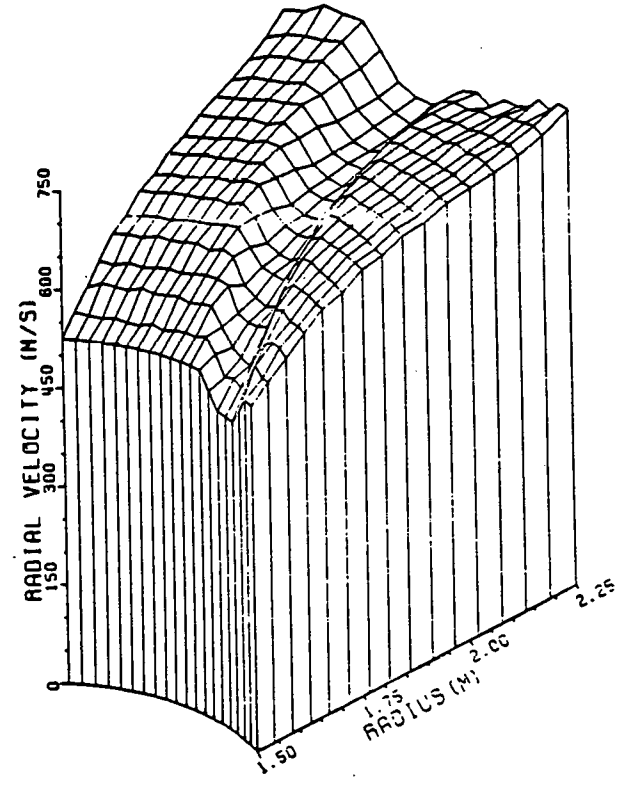

Fig. 5.4 Radial velocity component in outflow variation case.

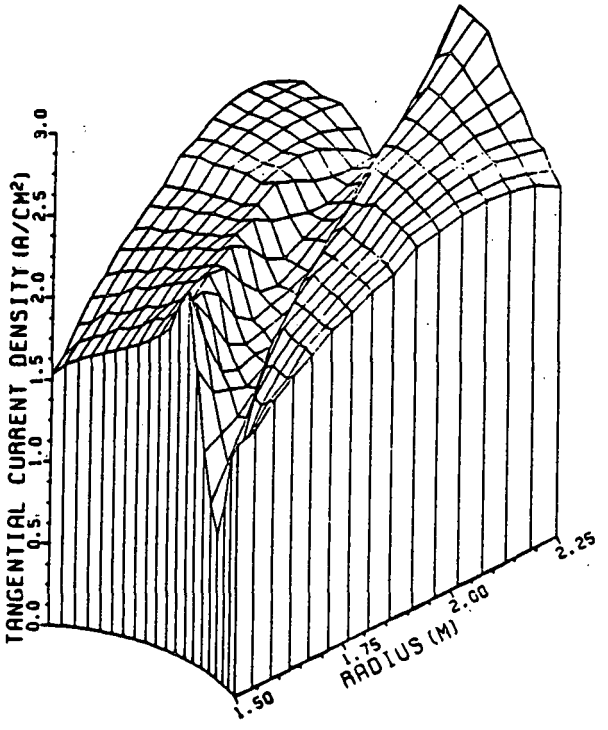

Fig. 5.5 Tangential current density in outflow variation case.

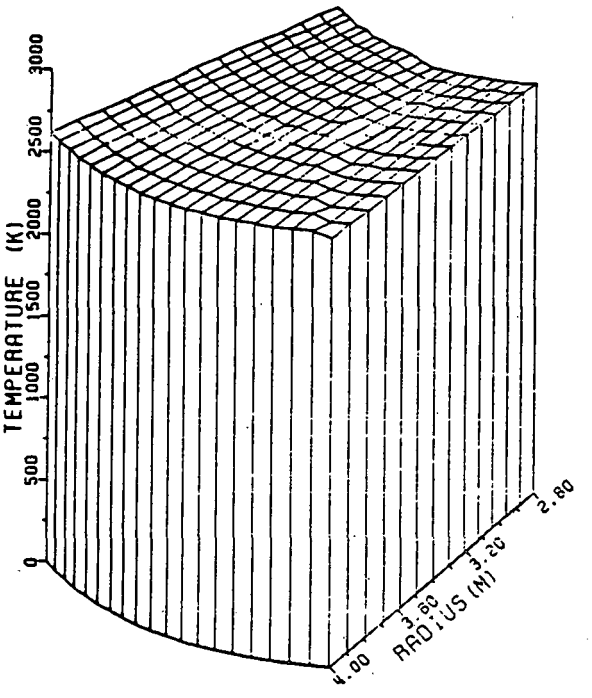

Fig. 5.6 Temperature in inflow variation case.

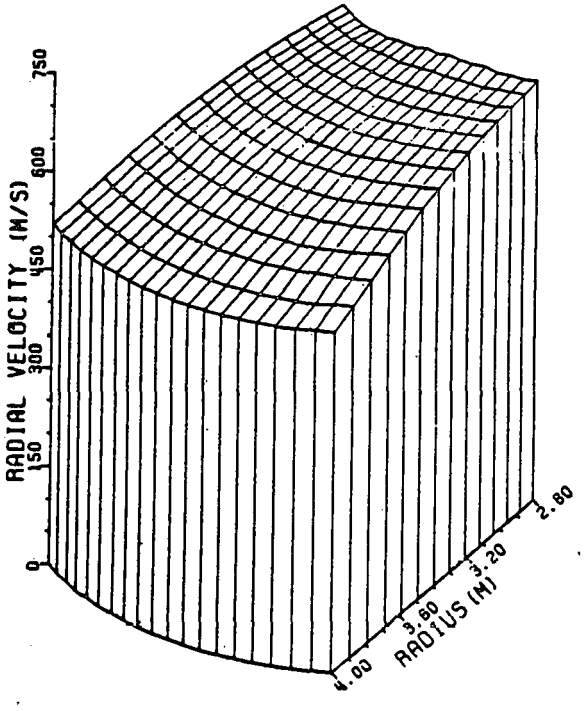

Fig. 5.7 Radial velocity component in inflow variation case.

concentration in the θ-direction will be undertaken. The results for laboratory scale calculations will be compared with experiment.

5.2 Performance Prediction Study

During the present reporting period progress was made in the performance prediction study. The overall generator performance of the inflow disk generator was calculated based on the results of a study in which each design element of the inflow disk generator, i.e., the combustor, the inlet flow path, the diffuser and the magnet was studied in detail [5.3].

The performance of generators of three different sizes (1250 MWth, 2000 MWth, 2500 MWth) was calculated for slagging wall channels and non-slagging hot wall (2000 K) channels. The properties of combustion gas were calculated under the combustion conditions given in Table 5.4. The channel performance was calculated by a quasi-one-dimensional code which takes into account the boundary layer velocity overshoot and the current leakage along the slag layer. A brief description of the method used to calculate the current leakage effect is given below.

Effect of Current Leakage Along the Slag Surface

The fluid mechanics and the thermal behavior of the molten slag layer in the MHD generator channel have been studied in the past, and the experimental data necessary to predict the thickness and the surface temperaure of the slag layer are available [5.4,5.5,5.6]. The surface temperature and the thickness of the slag layer are determined by the balance between the heat flux and the shear force exerted on the slag layer. The relation between the slag surface temperature T_s, the heat flux q and the shear force τ may be expressed as

$$T_s - T_{s,ref} = A \log_{10} (q/q_{ref}) + B \log_{10} (\tau/\tau_{ref}) \qquad (5.1)$$

Table 5.4

DESCRIPTION OF THE COMBUSTION GAS

Fuel:	Montana Rosebud Coal (5% moisture)
Air Preheat Temperature:	1800 K (No Oxygen Enrichment)
Combustor:	Two-stage cyclone
Equivalence Ratio	
First Stage:	2.0
Second Stage:	1.075
Ash Rejection Ratio:	0.775 (0.90 of liquid slag at first stage)
Seed:	K_2CO_3 (1% K by weight injected at the second stage)
Combustor Heat Loss:	0.04 of the thermal input (First stage .02; Second stage .02)
Combustor Exit Conditions	
P_{total}:	0.608 MPa
T_{total}:	2822 K

From the experimental data for the Montana Rosebud slag under the potassium seeded (.6 wt %) flow condition [5.5,5.6], the coefficients A, B and the reference properties were given as

$$A = 398 \text{ K} \qquad T_{s,ref} = 1725 \text{ K}$$

$$B = -164 \text{ K} \qquad q_{ref} = .48 \text{ MW/m}^2$$

$$\tau_{ref} = 62 \text{ N/m}^2$$

The temperature within the slag layer can be calculated readily from the heat flux as

$$T = T_s - \frac{q}{K_{slag}} \cdot y \tag{5.2}$$

where y is the distance from the slag surface into the layer. The thermal conductivity of the slag is considered to be constant, K_{slag} = 1.1 W/m·k [5.6]. The electrical conductivity of the slag σ_{slag} in the present analysis was deduced from the data obtained by Pollina and Larsen [5.7]. For the Montana Rosebud slag containing 13.8 wt% of K_2O the slag conductivity is expressed as

$$\log_{10} \sigma_{slag} = -.9445 \cdot 10^4/T + 6.404 \tag{5.3}$$

where σ_{slag} is in mho/m and T is in K.

The leakage current I_{leak} flowing within a slag layer at radius r can be calculated from Eqs. (5.1), (5.2), (5.3), and the electric field E as

$$I_{leak} = 2\pi r E \int_0^{\delta} \sigma_{slag}(y)\, dy \tag{5.4}$$

where δ is the slag thickness. The slag substrate temperature for the present study is taken to be 1000 K.

Generator Channel Performance

In calculating the generator channel performance, thermodynamic and electrical properties of the gas entering the channel were averaged in the tangential direction along the scroll. This is based on results of Reference [5.3] that the nonuniformities caused by losses in the inlet scroll do not introduce appreciable deterioration in performance. The magnet is of the split-pair type and the magnetic field strength exceeds 8 Tesla at outer radii of the channel, providing an ideal power generation condition for the inflow disk generator. The diffuser pressure recovery coefficient C_{PR} is taken to be 0.8. The choice of this relatively high value of C_{PR} for the inflow disk generator is justified because of the negligible inlet blockage and the effect of swirling flow in the conical diffuser. In order to account for the effect of boundary layer velocity overshoot, the friction coefficient obtained, based on the flat plate boundary layer model was multiplied by a factor which increases from 1.0 at the inlet to 2.5 at the exit. This simple correction is based on the result of a study in which effects of the velocity overshoot in the insulating wall boundary layer of a Faraday generator were investigated [5.8]. The Mach number in the channel is held constant at $M = 0.9$.

In Figs. 5.8 and 5.9 electrical and thermal properties along a 2000 MWth channel are shown. The sudden increase of E at the midpoint of the channel (Fig. 5.8) is caused by the current take-off by the intermediate electrode (see Fig. 5.10). This sudden increase of E causes an increase of the leakage current as shown in Fig. 5.9. The current leakage amounts to about 2.5% of the load current at the inlet of the generator channel and at the intermediate electrode position. The leakage current decreases sharply as the slag surface temperature goes down toward the freezing point at the exit of the channel. This large decrease of the slag surface temperature in the downstream of the channel is the result of the boundary layer velocity overshoot. Averaged over the entire channel, the slag current leakage amounts to about 1.5% of the load current.

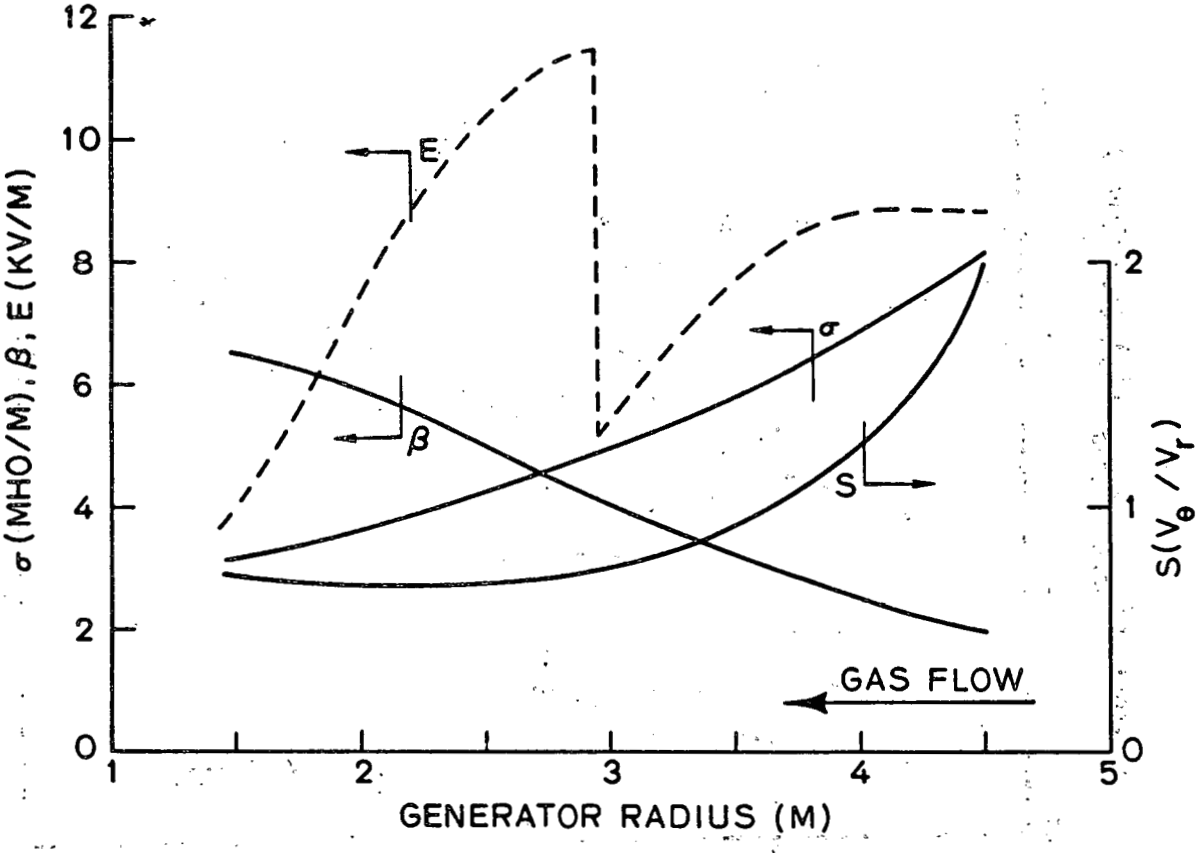

Figure 5.8 Electrical properties along a 2000 MW(th) inflow disk channel.

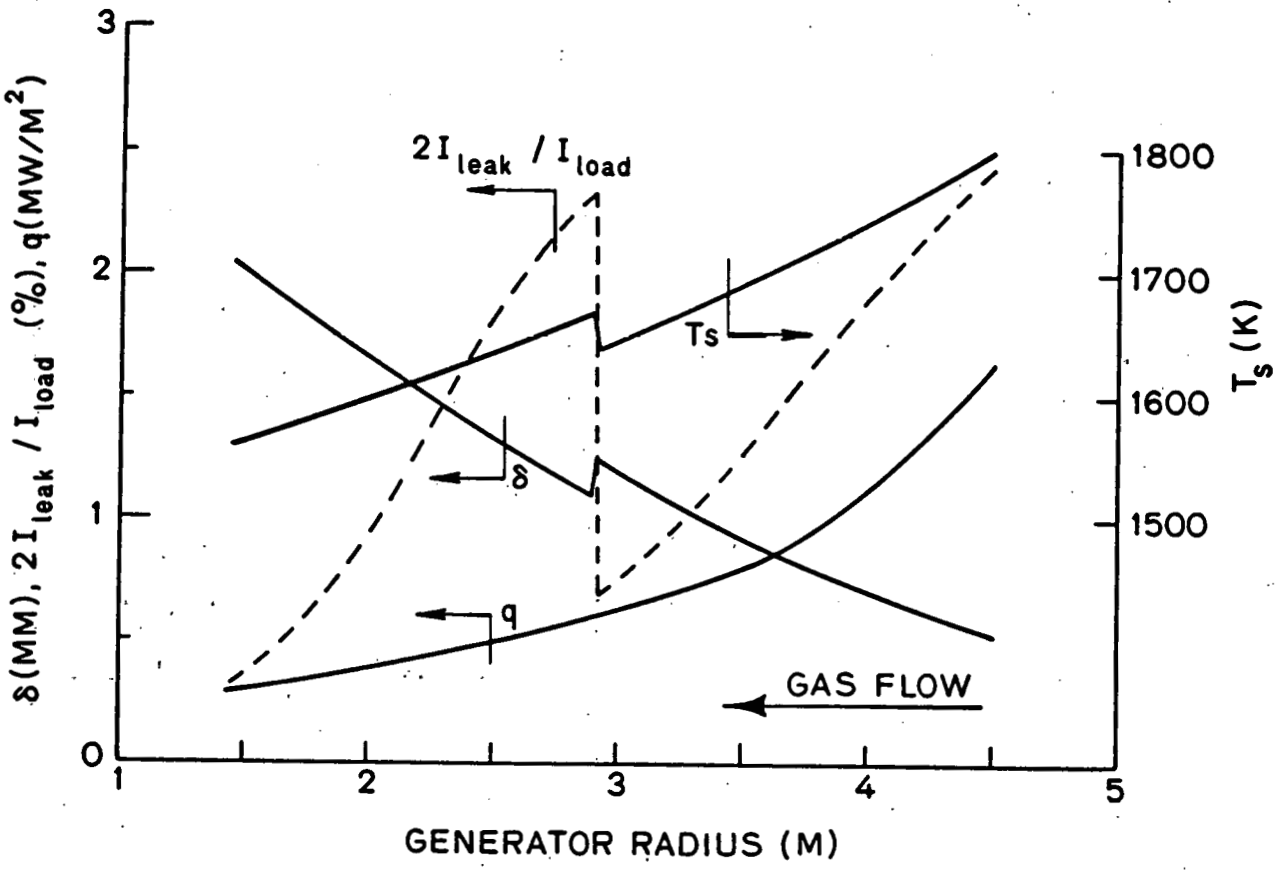

Figure 5.9 Thermal properties along a 2000 MW(th) inflow disk channel.

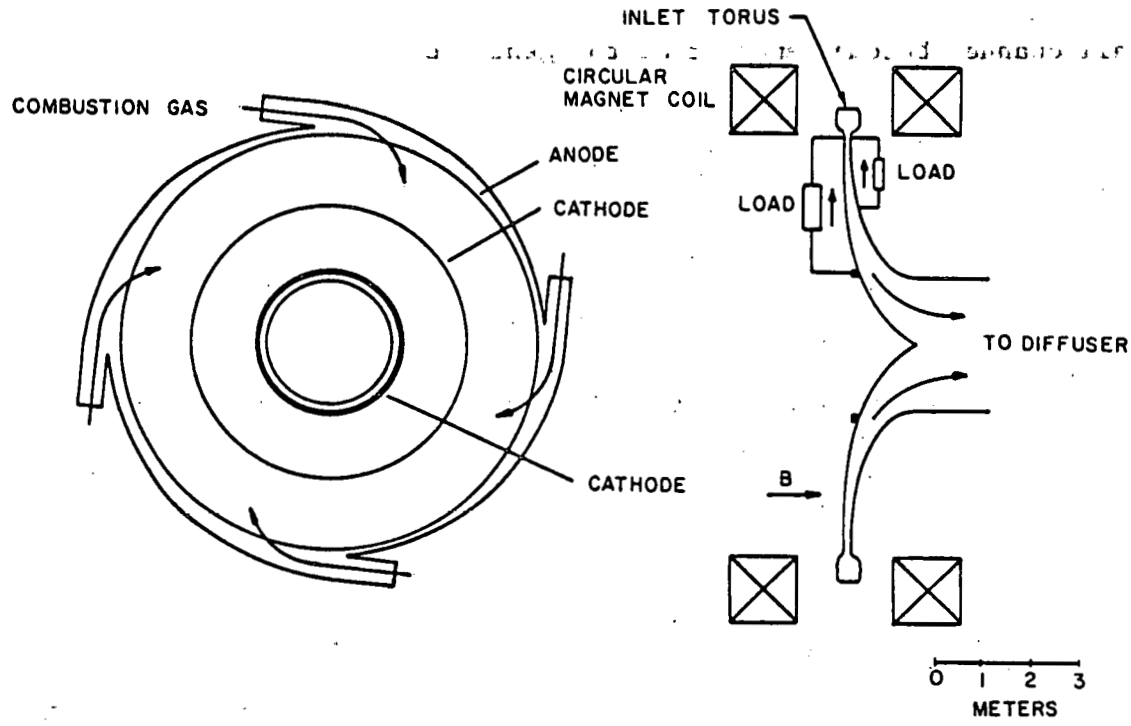

Figure 5.10 Conceptual design of a baseload inflow disk generator.

Table 5.5 summarizes the overall performance of the inflow disk generator for three different sizes. The enthalpy extraction of these generators is plotted against the input in Fig. 5.11. The difference between the performance of the hot wall channel and that of the slagging wall channel becomes smaller as the generator size increases.

The performance results obtained in this study are compared with the performance of linear generators in Fig. 5.12. The performance of linear generators was deduced from the data given in the baseload system studies available to date [5.8-5.13]. The combustion products of coal [5.8,5.13], char [5.8,5.11] and the residual oil [5.9,5.10,5.12] with preheated air at temperatures ranging from 1150°K to 1770°K are considered in these studies. The thermal input to such linear generators is from 1500 MW(th) [5.8,5.9,5.11] to 2000 MW(th) [5.9,5.10,5.12,5.13]. It should be emphasized that the performance of some linear generators was calculated based on more optimistic assumptions than those made in recent performance prediction studies. It is shown that the performance of the inflow disk generator is similar to that of the diagonal generator.

Table 5.5

OVERALL GENERATOR PERFORMANCE

Thermal Input (MW)	1250		2000		2500	
Combustor Exit						
Enthalpy Flow (MW)	2000		3200		4000	
Mass Flow (kg/s)	507		811		1014	
P_{tot} (MPa)	.608		.608		.608	
T_{tot} (K)	2822		2822		2822	
Inlet Flow Path	Slagging	Hot Wall (T_w=2000K)	Slagging	Hot Wall (T_w=2000K)	Slagging	Hot Wall (T_w=2000K)
Heat Loss (MW)	99.6	85.56	134.4	115.2	152.0	130.9
Generator Channel						
Inlet Swirl	2.0					
Mach Number	0.9					
B-Field (Tesla)	8.8 → 7.6					
Electrode Configuration	Three terminals (one anode and two cathodes, see Fig. 1)					
Average Electric Field (kv/m)	7.41	8.14	7.96	8.12	8.41	8.51
Channel Radius (m)	4.5→1.5	4.5→1.4	4.5→1.8	4.5→1.7	4.5→1.9	4.5→1.9
Channel Height (cm)	9.9→65	9.9→60	15→83	15→85	19→91	19→93
Electrical Output (MW)	358.0	372.0	603.2	618.2	768.8	779.6
Heat Loss (MW)	91.7	59.5	91.3	61.1	90.5	61.2
Overall Enthalpy Extraction	.179	.186	.189	.193	.192	.195
Isentropic Efficiency	.627	.651	.660	.677	.673	.683
Diffuser						
C_{PR}	0.8					
Exit Pressure (MPa)	.117					

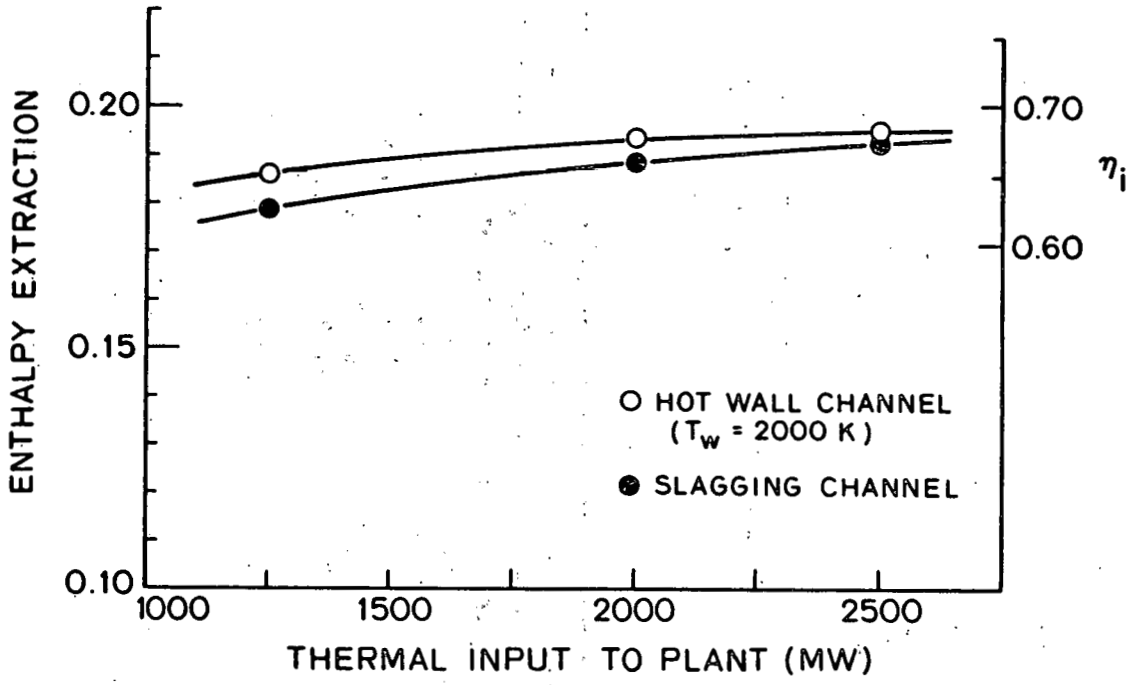

Figure 5.11 Enthalpy extraction of inflow disk generator.

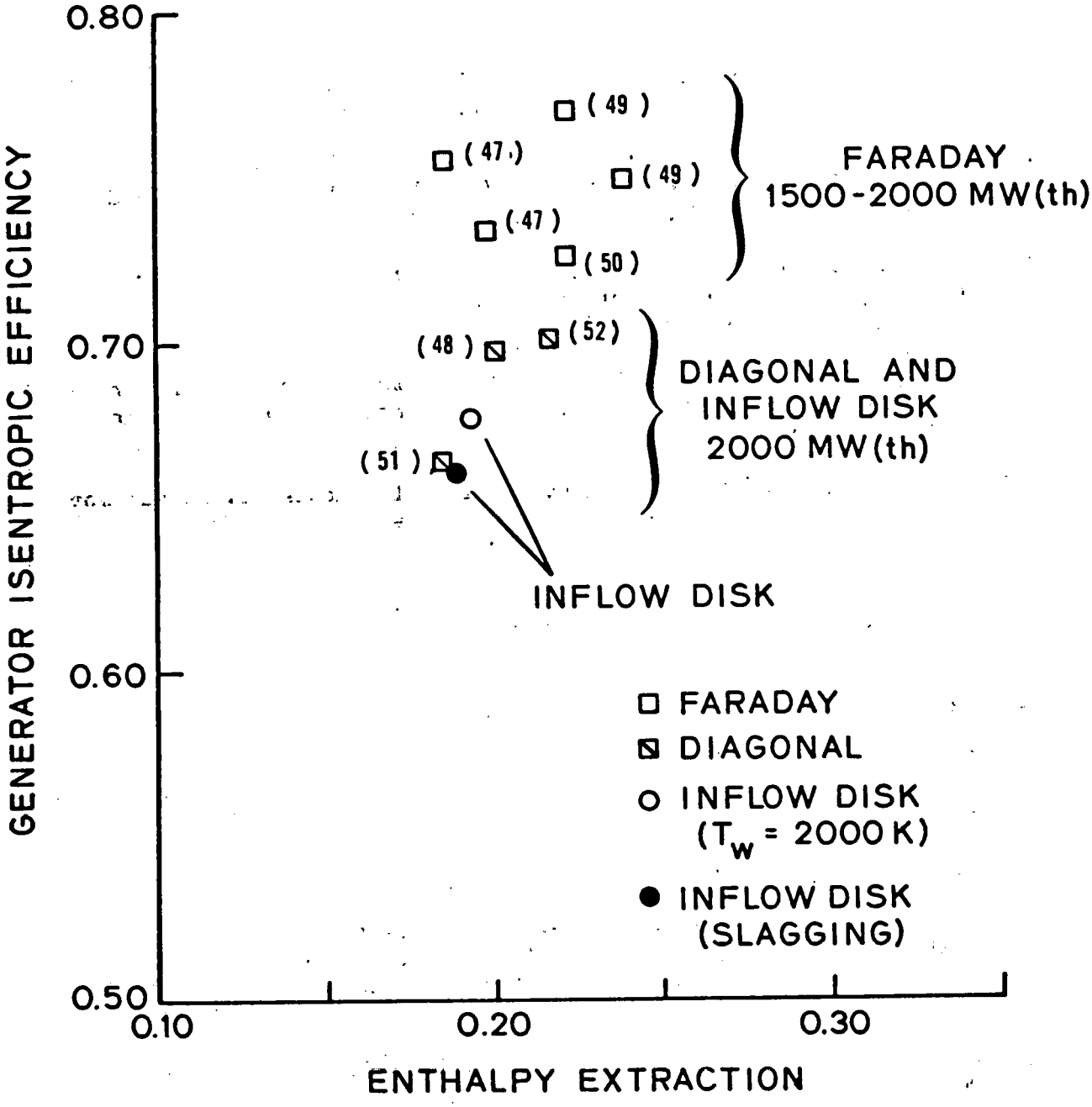

Figure 5.12 Comparison of the performance of the inflow disk generators with that of linear generators.

6.0 REFERENCES

2.1 Rosa, R. J., "The Hall and Ion Slip Effects in a Nonuniform Gas," Physics of Fluids, Vol. 5, No. 9, pp. 1081-1090, 1962.

2.2 "A High Magnetic Field MHD Generator Program," Annual Report FE-2341-13, for the period July 1, 1978 - June 30, 1979, Stanford University, pp. 24-29.

2.3 "A High Magnetic Field MHD Generator Program," Annual Report FE-15611-3, for the period October 1, 1979 - September 30, 1980, Stanford University, pp. 3-19.

2.4 "A High Magnetic Field MHD Generator Program," Quarterly Report FE-15611-4, for the period October 1 - December 31, 1980, Stanford University, pp. 3-7.

2.5 I. A. Vasil'eva, V. V. Kirillov, G. P. Malyuzhonok, I. A. Masimov, and V. B. Novosadov, "Measurements of Plasma Temperature by Spectroscopic Method with a Continuous Automatic Recording." High Temperature 11, No. 4 (1973). See also, Open Cycle Magnetohydrodynamic Power Generators, Eds. M. Petrick and B. Ya. Shumyatsky, Chap. 14, "Plasma Diagnostics in an MHD Installation," by S. A. Self, I. A. Vasil'eva and A. P. Nefedov.

3.1 Rankin, R. R., "Insulating Wall Boundary Layer in a Faraday MHD Generator," Department of Mechanical Engineering, Stanford University, April 1978.

3.2 Rankin, R. R., Self, S. A., Eustis, R. H., "Study of the Insulating Wall Boundary Layer in a Faraday MHD Generator," AIAA Journal, Vol. 18, No. 9, September 1980.

3.3 McLaughlin, D. K., Tiederman, W. G., "Biasing Correction for Individual Realization of Laser Anemometer Measurements in Turbulent Flows," Physics of Fluids, Vol. 16, No. 12, December 1973.

4.1 Unkel, W. C., "Axial Field Limitations in MHD Generators," HTGL Report No. 107, Stanford University, April 1978.

4.2 Daily, J. W., "Boundary Layer Phenomena in Combustion Driven MHD Power Generators," HTGL Report No. 102, Stanford University, December 1975.

4.3 James, R. K., "Joule Heating Effects in the Electrode Wall Boundary Layer of MHD Generators," HTGL Report No. 115, Stanford University, January 1980.

4.4 Oliver, D. A., "The Prediction of Inter-Electrode Breakdown in MHD Generators," 14th Symposium on Engineering Aspects of MHD.

4.5 Mitchner, M. and Kruger, C. H., Partially Ionized Gases, John Wiley and Sons, New York, 1973.

4.6 Zalkind, V. I., Kirillov, U. U., Tikhotsky, A. S., and Uspenskaya, G. L., "Experimental Investigation of Interelectrode Breakdown in MHD Channels," 7th International Conference on MHD Electrical Power Generation.

5.1 "A High Magnetic Field MHD Generator Program," Final Report FE-2341-16, for the period July 1, 1976 - December 31, 1979, Stanford University.

5.2 "A High Magnetic Field MHD Generator Program," Annual Report FE-15611-3, for the period October 1, 1979 - September 30, 1980, Stanford University.

5.3 "Feasibility of the Inflow Disk Generator for Open-Cycle MHD Power Generation," Final Report to EPRI, TPS 79-779, by High Temperature Gasdynamics Laboratory, Department of Mechanical Engineering, Stanford University, EPRI AP-1639, September 1980.

5.4 Koester, J. K., Rodgers, M. E. and Eustis, R. H., "In-Channel Observations on Coal Slag," 15th Symposium on Engineering Aspects of MHD, Philadelphia, May 1976, pp. I.6.1-I.6.10.

5.5 Rodgers, M. E., Ariessohn, P. C. and Kruger, C. H., "Comparison of Measurements and Predictions of the Fluid Mechanics and Thermal Behavior of MHD Channel Slag Layers," 16th Symposium on Engineering Aspects of MHD, Pittsburgh, May 1977, pp. VIII.4.26-31.

5.6 Rodgers, M. E. and Kruger, C. H., "Fluid Mechanics and Thermal Behavior of MHD Channel Slag Layers," 17th Symposium on Engineering Aspects of MHD, Stanford University, March 1978, p. C.2.1-C.2.6.

5.7 Pollina, R. and Larsen, R., "MHD Slag Electrical Conductivity Studies," 17th Symposium on Engineering Aspects of MHD, Stanford, March 1978, pp. C.6.1-C.6.6.

5.8 Rankin, Roy R., "Insulting Wall Boundary Layer in a Faraday MHD Generator," Topical Report, High Temperature Gasdynamics Laboratory, Mechanical Engineering Department, Stanford, University, April 1978.

5.9 Tsu, T. C., Young, W E. and Way, S., "Optimization Studies of MHD-Steam Plants," Proceedings of a Symposium on MHD Electrical Power Generation, Salzburg, July 1966, Vol. III, pp. 899-911.

5.10 Coney, M. W. E. and Heywood, J. B., "Some Design Considerations for a Single-Load Generator," Proceedings of a Symposium on MHD Electrical Power Generation, Warsaw, July 1968, Vol. IV, pp. 2687-2702.

5.11 Mori, Y., et al., "Cycle and Efficiency of Large Scale Open-Cycle MHD Power Plant," Fifth International Conference on MHD Electrical Power Generation, Munich, April 1971, Vol. I, pp. 569-584.

5.12 Way, S., "MHD Power Plant for Early Realization," Fifth International Conference on MHD Electrical Power Generation, Munich, April 1971, Vol. I, pp. 615-628.

5.13 Takano, K., Onda, K., and Mori, Y., "Calculation of Performances of Large Scale Diagonal MHD-Steam Plants," 13th Symposium on Engineering Aspects of MHD, Stanford University, March 1973, pp. V.6.1-V.6.9.

☆U.S. GOVERNMENT PRINTING OFFICE: 1981-740-145/2296